Water Waves
https://doi.org/10.1007/s42286-024-00084-4

ORIGINAL ARTICLE

A Study of Extreme Water Waves Using a Hierarchy of Models Based on Potential-Flow Theory

Junho Choi[1] · Anna Kalogirou[2] · Yang Lu[3] · Onno Bokhove[3] · Mark Kelmanson[3]

Received: 20 October 2023 / Accepted: 10 January 2024

Abstract

The formation of extreme waves arising from the interaction of three line-solitons with equal far-field amplitudes is examined through a hierarchy of water-wave models. The Kadomtsev–Petviashvili equation (KPE) is first used to prove analytically that its exact three-soliton solution has a ninefold maximum amplification that is achieved in the absence of spatial divergence. Reproducing this ninefold maximum paves the way for simulations based on both the Benney–Luke equations (BLE) and more advanced potential-flow equations (PFE). To preserve (for the sake of computations) the region of interaction, exact KPE solutions on an infinite domain are used to yield initial conditions that seed the BLE and PFE models within a periodic domain. The above strategies are realised by directly implementing the corresponding time-discretised variational principles within the finite-element environment *Firedrake*, one aim being automation of the generation of the algebraically cumbersome weak formulations. In the case of three-soliton interactions, it is found numerically that an amplification factor in the interval circa (7.6, 9) can be achieved within the BLE framework, whereas in the PFE framework, this falls to circa 7.8.

✉ Anna Kalogirou
Anna.Kalogirou@nottingham.ac.uk

✉ Onno Bokhove
O.Bokhove@leeds.ac.uk

Junho Choi
junho_choi@kaist.ac.kr

Yang Lu
mmyl@leeds.ac.uk

Mark Kelmanson
M.Kelmanson@leeds.ac.uk

1 School of Mathematical Sciences, Korea Advanced Institute of Science and Technology, Daejeon 34141, South Korea

2 School of Mathematical Sciences, University of Nottingham, Nottingham NG7 2RD, UK

3 School of Mathematics, University of Leeds, Leeds LS2 9JT, UK

Published online: 15 February 2024

Keywords Rogue waves · Potential-flow simulations · Kadomtsev–Petviashvili solution · Web-solitons

1 Introduction

Water-wave motion is ubiquitous and can be observed most easily on rivers, on canals, on lakes, at the beach and at sea. Understanding water-wave dynamics is important, since waves impacting on shores and structures can have destructive effects, both on the natural barriers protecting human habitation and on man-made infrastructures. Industrial maritime-engineering structures at sea, such as ships, offshore wind-turbines, and offshore oil platforms, need to be sufficiently robust to endure considerable periods under wave impact. Wave impact by extreme or rogue water waves can be particularly detrimental due to their large amplitude and sudden appearance [1], all of which motivates their study. Additionally, such rogue waves are fascinating to watch in their own right, leading to the straightforward question studied here: how can we model and generate maximum-amplitude water waves from incoming waves of equal amplitude on an open or periodic horizontal plane?

A water wave is considered extreme when its height H exceeds twice the significant wave height H_s of the ambient waves [2]. Wave height therein refers to the vertical distance from the wave trough to the wave crest. The significant wave height H_s was originally defined as the wave height of the highest third of the ambient waves, a definition later replaced as being four times the standard deviation of the surface elevation [2]. Such rogue waves are statistically rare and concern waves in the tail of the wave-height distribution with wave heights larger than $2H_s$. Investigations of extreme or rogue waves involve, on the one hand, observational analysis and simulation of wave statistics [3–5]; on the other, extreme-wave heights can be observed and calculated exactly and deterministically when multiple solitonic or cnoidal waves interact as crossing waves, or in seas with the highest wave peaks emerging where the separate linear segments of the wave crests cross in a nonlinear fashion; see e.g. [6].

Exact solutions of such waves have been derived for the Kadomtsev–Petviashvili equation (KPE) [7], which is an asymptotic model equation of the more advanced potential-flow water-wave equations (PFE), with the KPE modelling the free-surface elevation of the water in two horizontal spatial dimensions X and Y and time τ (dimensionless variables). Within the KPE, the lateral Y-dependence of the dynamics is asymptotically weak and only unidirectional wave propagation in the X-direction is retained. The PFE are in turn an approximation to the incompressible Navier–Stokes equations with a free water surface, or to the more complex two-phase fluid equations, the latter modelling both air and water as well as their smooth or broken interface(s). Within the present context, the PFE are considered as parent equations representing reality, with possible wave-breaking parameterised in a phenomenological fashion [8]. Various intermediate-complexity asymptotic water-wave models between KPE and PFE exist, concerning either unidirectional or bidirectional wave propagation in the two horizontal dimensions. Bidirectional water-wave models generally require numerical modelling to analyse their solutions. We have in particular considered the bidirectional Benney–Luke equations (BLE) [9, 10], both because the BLE are often

used as an interim step to derive and assess solutions of the KPE [11], and because the BLE are readily discretised numerically in a geometric (and, as such, consistent) manner via a straightforwardly available variational principle (VP) [12]. Consistent variational discretisations are deemed important for investigating maximum-wave amplification, because wave amplitude can be preserved in such so-called compatible or geometric numerics, which preservation is tied to energy conservation as well as to other conservation laws. In summary, we remark that the BLE are more advanced and realistic than the KPE, and that the PFE in turn improve upon the BLE.

Inspired by the aforementioned statistical and deterministic extreme-wave analyses, we have investigated how realistic are some extreme-solitonic wave interactions modelled with KPE [13]. For the KPE, we have assessed analytically the maximal attainable amplitude of three interacting solitons, with each individual soliton having an archetypical sech-profile amplitude of the same magnitude in its far field. The three-soliton solution is achieved by two pairs of interacting solitons, both of which in separation constitute a travelling-wave O-type (2, 2)-line soliton solution (according to Kodama's classification [14]) that is steady in its frame of reference. Even though such three-soliton interactions have been hitherto analysed, exact analysis establishing the maximum amplification factor of nine appeared to be missing, so it is presented fully herein. In contrast to the better-known two-soliton interaction with ever-present maximally fourfold amplification, the maximum for the three-soliton case is achieved at one point (X^*, Y^*, τ^*) in space and time, since the two pairs of two-soliton solutions collide under an optimal angle and their combination is unsteady. Such an analysis is required, because we seed the BLE with the exact KPE solution at a time prior to the maximum wave-peak occurrence to assess the wave coherence at later times in the more complex BLE. Hence, we are able to assess numerically what maximum amplification is attainable for the more realistic BLE. However, such an approach has at least two shortcomings that the present work now aims to address.

The maximum ninefold amplification is achievable only in the vanishing limit $\delta \to 0$ of a small parameter δ that is proportional to the difference of the two smallest of three (positive) wavenumber parameters, with the remaining three wavenumbers being equal and opposite to the three main ones. In that limit, the Y-location of the maximum was shown to diverge in our earlier calculations, with $Y^* \to -\infty$, while $X^* = \tau^* = 0$. As a consequence, the numerical simulation of the BLE was seeded with an exact solution of the KPE for a finite-yet-small value of δ to avoid this divergence: we took the value $\delta \approx 0.0014$ in [13]. The KPE seed was taken at a time prior to the growing phase from its intermediate-in-time fourfold to ninefold maximum. That value of δ relates to a particular maximum amplification of 8.4 for the KPE, while the numerical simulation of BLE gave an amplification of approximately 7.8.

Consequently, our first goal is to improve the analysis of the maximum amplification and to slow down or to avert divergence of its space-time location Y^*. Additionally, we aim to show how to seed the BLE and PFE with an initial condition of higher order accuracy in the amplitude and dispersion parameters, respectively, denoted by ϵ and μ. A key step towards the second goal is to modify the non-periodic velocity potential valid on an infinite plane, such that the dynamics fit within a (more computationally convenient) X-periodic domain, which approximation is possible due the symmetry of the solutions. This minor alteration of the domain in effect turns the solitonic dynamics

into cnoidal-wave dynamics in which the maximum amplification in the interior of the domain is hardly (as quantified in the results below) affected by periodicity effects at the boundaries.

As such, our second goal is to numerically assess the maximum amplification attainable in the more realistic PFE and to compare these PFE-based amplifications with new higher order ones using the BLE. Effects that will limit the amplification of the three interacting solitons in the PFE are as follows: dispersive effects will lead to wave-spreading and lower amplitudes; higher amplitude waves will break, thereby lowering wave amplitudes; and the numerical modelling for the PFE will be much more demanding than that for the BLE.

To achieve high-level (as defined below) and consistent simulations of the PFE, we have built a new three-dimensional solver based on implementing a suitable time-discrete variational principle (VP) of potential-flow dynamics directly into the finite-element environment *Firedrake* for solving partial differential equations [15]. Essentially, a modification of Luke's variational principle for water waves [16] is formulated. Rather than manually implementing consistent-yet-cumbersome weak formulations of the PFE, Firedrake automatically generates these from the relevant time-discrete VP, whereupon in-built Firedrake solvers and parallelised simulations are readily defined and available for higher order spatial discretisations. Generally, for these demanding nonlinear wave motions, we need at least quadratic-polynomial approximations in space and second-order accuracy in time. The spatial accuracy in Firedrake can be varied easily and independently in the horizontal and vertical directions, and the default-implemented Gauss–Lobatto–Legendre (GLL) polynomials are spectrally accurate. Such a versatile high-level approach—namely Firedrake's intrinsic use of time-discrete VPs—reduces development time, eradicates manual-derivation errors, and allows straightforward modification to accommodate dynamics within an X-periodic domain. Moreover, the numerical implementation is tightly connected to the mathematical formulation, since the employed unified form language (UFL) *is fully decomposable*. In plain terms, this means that a nearly phonetic translation of the relevant formulas of the variational principle establishes a working code for the wave dynamics. Both second-order modified-midpoint and Störmer–Verlet time discretisations have been defined and tested for both BLE and PFE. The novel codes were carefully constructed and verified, first for a single travelling soliton, then further developed for the more advanced two- and three-soliton interactions of interest. Within this environment, simulations using over 2 million degrees-of-freedom have allowed the wave science to commence, while solver optimisation remains ongoing. We remark that optimisation relies heavily on PETSc solvers of the relevant linear and nonlinear algebraic systems [17, 18].

In summary, the above-described computer-science approach to solving complicated wave dynamics within Firedrake forms a third novel goal of our work. The VP-based strategy includes and extends earlier work based on discretising the weak formulations following from discretised variational principles, including approaches in which: (i) the mesh is moved according to the free-surface movement [19, 20]; and (ii) the computational domain is fixed after a coordinate transformation and only one element is used in the vertical direction, combined with higher order Lagrange polynomials (implemented within Firedrake) [21, 22]. Both of these previous approaches

used first-order piecewise-linear continuous Galerkin polynomials (denoted as CG1, at least in the horizontal), while the current approach runs with the necessary higher order GLL polynomials, typically CG2 or higher.

As a result of the above, the following outlook of the current paper emerges. In Sect. 2, the hierarchy of the three wave models—PFE, BLE, and KPE—is introduced, including the two scalings involved. KPE and BLE are established in different dimensionless coordinates, while we keep the dimensional form of the PFE, essentially using SI-units as (hidden) scaling in the PFE computations. The extended analysis—of the maximum amplification of three-soliton interaction in KPE—is undertaken in Sect. 3, pertaining to our first goal. The numerical modelling tools are set up in Sect. 4 and detail the computer-science novelty, i.e., our third goal. Simulations results of BLE and PFE are discussed, compared, and analysed in Sect. 5, pertaining to our second goal. We finish with concluding remarks in Sect. 6.

2 Hierarchy of Potential-Flow, Benney–Luke, and Kadomtsev–Petviashvili Equations

To create initial conditions for the Benney–Luke equations (BLE) and the potential-flow equations (PFE), we consider the formal link from the PFE via the BLE to the Kadomtsev–Petviashvili equation (KPE). The PFE in dimensional spatial–temporal coordinates $(x, y, z, t \geq t_0)$ and variables are given by

$$\Delta\phi + \partial_{zz}\phi = 0 \quad \text{in } \Omega \subset \mathbb{R}^3, \tag{1a}$$

$$\partial_t \eta + \nabla\phi \cdot \nabla\eta - \partial_z\phi = 0 \quad \text{at } z = H_0 + \eta, \tag{1b}$$

$$\partial_t \phi + \frac{1}{2}|\nabla\phi|^2 + \frac{1}{2}(\partial_z\phi)^2 + g\eta = 0 \quad \text{at } z = H_0 + \eta, \tag{1c}$$

$$\mathbf{n} \cdot \nabla\phi = 0 \quad \text{on } \partial\Omega_s, \tag{1d}$$

$$\partial_z\phi = 0 \quad \text{at } z = 0, \tag{1e}$$

where $\phi = \phi(x, y, z, t)$ is the velocity potential and $\eta = \eta(x, y, t)$ is the deviation from the rest surface with H_0 the rest depth. Here, the gradient is in two spatial dimensions, $\nabla = (\partial_x, \partial_y)^T$, and $\Delta = \nabla^2$. Also, the Laplace equation is satisfied in a three-dimensional domain Ω with boundary $\partial\Omega$, with Ω_s denoting solid-wall boundaries. We can formally derive the BLE from (1) using the non-dimensional variables

$$\widehat{x} = \frac{\sqrt{\mu}}{H_0}x, \quad \widehat{y} = \frac{\sqrt{\mu}}{H_0}y, \quad \widehat{z} = \frac{1}{H_0}z, \quad \widehat{t} = \frac{\sqrt{gH_0\mu}}{H_0}t,$$
$$\widehat{\eta} = \frac{1}{\epsilon H_0}\eta, \quad \widehat{\phi} = \frac{\sqrt{\mu}}{\epsilon H_0\sqrt{gH_0}}\phi, \tag{2}$$

with amplitude parameter $\epsilon = a/H_0 \ll 1$ and dispersion parameter $\mu = (H_0/\lambda)^2 \ll 1$; here, λ is a typical wavelength. Herein, we denote the seabed potential at $\widehat{z} = 0$ by

$$\Phi(\widehat{x},\widehat{y},\widehat{t}) := \widehat{\phi}(\widehat{x},\widehat{y},0,\widehat{t}). \tag{3}$$

In the derivation of the BLE, e.g., see [12] and references therein, $\widehat{\phi}$ has a Taylor expansion in terms of $\widehat{z}$ as follows:

$$\widehat{\phi}(\widehat{x},\widehat{y},\widehat{z},\widehat{t}) = \Phi(\widehat{x},\widehat{y},\widehat{t}) - \frac{\mu}{2}\widehat{z}^2\widehat{\Delta}\Phi + \frac{\mu^2}{24}\widehat{z}^4\widehat{\Delta}^2\Phi + \mathcal{O}(\mu^3\widehat{z}^6). \tag{4}$$

Upon using (2) and substituting (4) into (1), and after truncating terms up to order $\mathcal{O}(\epsilon^2\mu, \epsilon^3)$, the BLE emerge—in the non-dimensional coordinates $(\widehat{x},\widehat{y},\widehat{t} \geq \widehat{t}_0) \in \mathbb{R}^3$ for some initial time $\widehat{t}_0$—as follows:

$$\partial_{\widehat{t}}\widehat{\Phi} - \frac{\mu}{2}\partial_{\widehat{t}}\nabla^2\widehat{\Phi} + \frac{\epsilon}{2}|\nabla\widehat{\Phi}|^2 + \widehat{\eta} = 0 \quad \text{in } \widehat{\Omega}_h \subset \mathbb{R}^2, \tag{5a}$$

$$\partial_{\widehat{t}}\widehat{\eta} - \frac{\mu}{2}\partial_{\widehat{t}}\nabla^2\widehat{\eta} + \nabla\cdot\left((1+\epsilon\widehat{\eta})\,\nabla\widehat{\Phi}\right) - \frac{2}{3}\mu\nabla^4\widehat{\Phi} = 0 \quad \text{in } \widehat{\Omega}_h, \tag{5b}$$

$$\mathbf{n}\cdot\nabla\widehat{\Phi} = 0 \quad \text{on } \partial\widehat{\Omega}_h, \tag{5c}$$

$$\mathbf{n}\cdot\nabla(\nabla^2\widehat{\Phi}) = 0 \quad \text{on } \partial\widehat{\Omega}_h. \tag{5d}$$

System (5) is valid in a two-dimensional domain $\widehat{\Omega}_h$ with boundary conditions stated at solid-wall boundaries $\partial\widehat{\Omega}_h$ (hats have been omitted from the gradients). We note that the BLE system has energy defined by

$$E(t) = \int_{\widehat{\Omega}_h}\left[\frac{1}{2}\widehat{\eta}^2 + \frac{1}{2}(1+\epsilon\widehat{\eta})|\nabla\widehat{\Phi}|^2 + \frac{\mu}{3}(\nabla^2\widehat{\Phi})^2\right]\mathrm{d}\widehat{x}\,\mathrm{d}\widehat{y}, \tag{6}$$

which is conserved over time (for the proof, see [13]). To formally derive the KPE from the BLE, see [6, 12], a new scaling is introduced as

$$X = \sqrt{\frac{\epsilon}{\mu}}\left(\frac{3}{\sqrt{2}}\right)^{1/3}(\widehat{x}-\widehat{t}), \quad Y = \frac{\epsilon}{\sqrt{\mu}}\left(\frac{3}{\sqrt{2}}\right)^{2/3}\widehat{y}, \quad \tau = \epsilon\sqrt{\frac{2\epsilon}{\mu}}\,\widehat{t}, \tag{7a}$$

$$\widehat{\Phi} = \sqrt{\epsilon}\left(\frac{2^5}{3^4}\right)^{1/6}\left(\Psi + \mathcal{O}(\epsilon^2)\right), \tag{7b}$$

with $\mu = \mathcal{O}(\epsilon^2)$ and additionally

$$u = \partial_X\Psi. \tag{7c}$$

A series of transformations[1] results in the well-known KPE [7] in "standard" form

$$\partial_X\left(4\partial_\tau u + 6u\partial_X u + \partial_{XXX}u\right) + 3\partial_{YY}u = 0. \tag{8}$$

[1] For completeness, further details are found in Appendix A; see also [23] and references therein.

According to KPE theory, cf. [14], a (web-soliton) solution can be set up via Hirota's transformation

$$u(X, Y, \tau) \equiv 2\partial_{XX} \ln\{K(X, Y, \tau)\}, \tag{9}$$

in which the function $K(X, Y, \tau)$ is a Wronskian whose elements satisfy a linear system of equations; this interim function K is defined later for the particular two- and three-soliton interactions investigated analytically and numerically in the ensuing sections.

Given this exact solution of the KPE, we define

$$\Psi(X, Y, \tau) \equiv 2\partial_X \ln\{K(X, Y, \tau)\} \tag{10}$$

and substitute Ψ into (7c), whence relations (5a) or (A1) yield the asymptotic BLE solutions

$$\widehat{\eta} \equiv \left(\frac{4}{3}\right)^{1/3} u + \epsilon \left[-\left(\frac{2^8}{3^4}\right)^{1/6} \partial_\tau \Psi - \left(\frac{3^2}{2^4}\right)^{1/6} \partial_X^3 \Psi - \left(\frac{2^2}{3^4}\right)^{1/6} (\partial_X \Psi)^2 \right], \tag{11a}$$

$$\widehat{\Phi} \equiv \sqrt{\epsilon} \left(\frac{4\sqrt{2}}{9}\right)^{1/3} \Psi, \tag{11b}$$

which are accurate to $\mathcal{O}(\epsilon^2)$.

Upon employing Eq. (11) for $\tau = \tau_0$ or $\widehat{t} = \widehat{t}_0 = \tau_0\sqrt{\mu/(2\epsilon)}/\epsilon$ via (7a), the dimensionless initial condition for the BLE emerges from the exact KPE solution, evaluated at a suitable time, as

$$\widehat{\eta}_0(\widehat{x}, \widehat{y}) = \widehat{\eta}(\widehat{x}, \widehat{y}, \widehat{t}_0) \quad \text{and} \quad \Phi_0(\widehat{x}, \widehat{y}) = \Phi(\widehat{x}, \widehat{y}, \widehat{t}_0). \tag{12}$$

Moreover, by applying (2) and (4) in (12), the corresponding (asymptotic and dimensional) initial conditions for the PFE at $t = t_0$ become

$$\eta(x, t, t_0) \equiv \eta_0(x, y) = \epsilon H_0 \widehat{\eta}_0(\widehat{x}, \widehat{y}), \tag{13a}$$

$$\phi_0(x, y) = \frac{\epsilon H_0 \sqrt{g H_0}}{\sqrt{\mu}} \left(\widehat{\Phi}_0(\widehat{x}, \widehat{y}) - \frac{\mu}{2} \widehat{z}_0^2 \widehat{\Delta} \widehat{\Phi}_0 + \frac{\mu^2}{24} \widehat{z}_0^4 \widehat{\Delta}^2 \widehat{\Phi}_0 \right), \tag{13b}$$

where $\widehat{z}_0(x, y) = \big(H_0 + \eta_0(x, y)\big)/H_0$ and $\phi(x, y, \eta_0(x, y), t_0) \equiv \phi_0(x, y)$. In what follows, we use the initialisations only to $\mathcal{O}(1)$ in ϵ for $\widehat{\eta}$, and hence to $\mathcal{O}(\epsilon)$ for η.

3 Maximum Amplification for Three-Soliton Interactions

In this section, we prove the ninefold maximum amplification by extending and correcting the preliminary proof in [13], but without imposing assumptions (as we did

in [13]) on the wave shifts. Instead, we choose any shift-inducing constants arising in the solutions in such a way that the time and spatial location at which the maximum occurs remain finite when $\delta \to 0$.

The proof provided unfolds in several stages, as follows:

- A solution $u(X, Y, \tau)$ for the KPE will be developed with three equal-amplitude sech-solitons in the far field. This far-field amplitude of each soliton is denoted by $\tilde{A}$. We will show that the solution is symmetric around $Y = Y^*$, i.e., that its dependence on Y contains only even functions of the argument $Y - Y^*$, as can also be discerned from the symmetry of the set-up; in this sense, the present work extends (50, 51) in [13].
- The candidate point of maximum amplification (X^*, Y^*, τ^*) is derived geometrically by considering the five centrelines of the three far-field line-solitons, due to a phase shift in the region of soliton interactions.[2]
- Given this ansatz for (X^*, Y^*, τ^*), and its symmetry around $Y = Y^*$, the computer-algebra environment `Maple` is used to show unambiguously that the maximum amplification factor $u(X^*, Y^*, \tau^*)/\tilde{A}$ occurs at this candidate point as a function of a parameter $\delta \geq 0$, in the limit $\delta \to 0$ of which $u(X^*, Y^*, \tau^*)/\tilde{A} \to 9$. Additionally, the Y^*-location remains finite for certain parameters $a, c \neq 1$ and $b = 1$ involved, in contrast to the $a = b = c = 1$ case considered in [13] which resulted in $Y^* \to -\infty$ in the vanishing-δ limit.

3.1 Three-Soliton Solution and Its *Y*-Symmetry

The function $K(X, Y, \tau)$ used in (9), e.g., see [13] and references therein, reads

$$\begin{aligned} K(X, Y, \tau) = {} & A_{135}\, e^{\theta_{135}} + A_{246}\, e^{\theta_{246}} + A_{235}\, e^{\theta_{235}} + A_{245}\, e^{\theta_{245}} \\ & + A_{136}\, e^{\theta_{136}} + A_{146}\, e^{\theta_{146}} + A_{236}\, e^{\theta_{236}} + A_{145}\, e^{\theta_{145}}, \end{aligned} \tag{14}$$

where $\theta_{ijk} = (k_i + k_j + k_k)X + (k_i^2 + k_j^2 + k_k^2)Y - (k_i^3 + k_j^3 + k_k^3)\tau$, in which the eight terms have been ordered pairwise and the six coefficients k_i, k_j, k_k are defined by (in which we assume three equal-amplitude solitons in the far field)

$$k_6 = -k_1 = \frac{1}{2}\tan\theta + \sqrt{\tilde{A}/2} = \sqrt{\tilde{A}}\left(\sqrt{2} + \sqrt{1/2} + \delta\right), \tag{15a}$$

$$k_5 = -k_2 = \frac{1}{2}\tan\theta - \sqrt{\tilde{A}/2} = \sqrt{\tilde{A}}\left(\sqrt{1/2} + \delta\right), \tag{15b}$$

$$k_4 = -k_3 = \sqrt{\tilde{A}/2}. \tag{15c}$$

The coefficients in (14) are functions of the k_i and are defined as follows:

$$A_{135} = (k_3 k_5^2 - k_5 k_3^2 - k_1 k_5^2 + k_1 k_3^2 + k_5 k_1^2 - k_3 k_1^2), \tag{16a}$$

[2] This revisited geometric argument corrects one given in [13], where an incomplete argument was used for the correct expression (34) in [13]; typos in (33b) of [13] are corrected here.

$$A_{235} = a\,(k_3k_5^2 - k_5k_3^2 - k_2k_5^2 + k_2k_3^2 + k_5k_2^2 - k_3k_2^2), \tag{16b}$$
$$A_{136} = c\,(k_3k_6^2 - k_6k_3^2 - k_1k_6^2 + k_1k_3^2 + k_6k_1^2 - k_3k_1^2), \tag{16c}$$
$$A_{236} = a\,c\,(k_3k_6^2 - k_6k_3^2 - k_2k_6^2 + k_2k_3^2 + k_6k_2^2 - k_3k_2^2), \tag{16d}$$
$$A_{145} = b\,(k_4k_5^2 - k_5k_4^2 - k_1k_5^2 + k_1k_4^2 + k_5k_1^2 - k_4k_1^2), \tag{16e}$$
$$A_{245} = a\,b\,(k_4k_5^2 - k_5k_4^2 - k_2k_5^2 + k_2k_4^2 + k_5k_2^2 - k_4k_2^2), \tag{16f}$$
$$A_{146} = b\,c\,(k_4k_6^2 - k_6k_4^2 - k_1k_6^2 + k_1k_4^2 + k_6k_1^2 - k_4k_1^2), \tag{16g}$$
$$A_{246} = a\,b\,c\,(k_4k_6^2 - k_6k_4^2 - k_2k_6^2 + k_2k_4^2 + k_6k_2^2 - k_4k_2^2), \tag{16h}$$

where a, b, c are positive constants that shift the location of the solution (with $a = b = c = 1$ corresponding to no shift). Using the skew symmetries $k_1 = -k_6$, $k_2 = -k_5$, $k_3 = -k_4$ with $k_6 > k_5 \geq k_4 > 0$, the coefficients (16) can (recalling the pairings in (14)) be simplified as follows:

$$A_{135} = -k_4k_5^2 - k_5k_4^2 + k_6k_5^2 - k_6k_4^2 + k_5k_6^2 + k_4k_6^2 \tag{17a}$$
$$A_{246} = a\,b\,c\,(k_4k_6^2 - k_6k_4^2 + k_5k_6^2 - k_5k_4^2 + k_6k_5^2 - k_4k_5^2) = a\,b\,c\,A_{135} \tag{17b}$$
$$A_{235} = 2\,a\,k_5(k_5^2 - k_4^2) \tag{17c}$$
$$A_{245} = 2\,a\,b\,k_5(k_5^2 - k_4^2) = b\,A_{235} \tag{17d}$$
$$A_{136} = 2\,c\,k_6(k_6^2 - k_4^2) \tag{17e}$$
$$A_{146} = 2\,b\,c\,k_6(k_6^2 - k_4^2) = b\,A_{136} \tag{17f}$$
$$A_{236} = a\,c\,(-k_4k_6^2 - k_6k_4^2 + k_5k_6^2 - k_5k_4^2 + k_6k_5^2 + k_4k_5^2) \tag{17g}$$
$$A_{145} = b\,(k_4k_5^2 - k_5k_4^2 + k_6k_5^2 - k_6k_4^2 + k_5k_6^2 - k_4k_6^2) = b\,A_{236}/(a\,c). \tag{17h}$$

The dominant terms in $K(X, Y, \tau)$ in the far field of the four quadrants are as follows:

$$K_{[1,2]^-} \approx A_{135}\,\mathrm{e}^{\theta_3+\theta_5}\left(\mathrm{e}^{\theta_1} + \frac{A_{235}}{A_{135}}\mathrm{e}^{\theta_2}\right) \quad \text{for } X < 0,\ Y \to -\infty \tag{18a}$$
$$K_{[5,6]^-} \approx A_{135}\,\mathrm{e}^{\theta_1+\theta_3}\left(\mathrm{e}^{\theta_5} + \frac{A_{136}}{A_{135}}\mathrm{e}^{\theta_6}\right) \quad \text{for } X < 0,\ Y \to \infty \tag{18b}$$
$$K_{[5,6]^+} \approx A_{245}\,\mathrm{e}^{\theta_2+\theta_4}\left(\mathrm{e}^{\theta_5} + \frac{A_{246}}{A_{245}}\mathrm{e}^{\theta_6}\right) \quad \text{for } X > 0,\ Y \to -\infty \tag{18c}$$
$$K_{[1,2]^+} \approx A_{146}\,\mathrm{e}^{\theta_4+\theta_6}\left(\mathrm{e}^{\theta_1} + \frac{A_{246}}{A_{146}}\mathrm{e}^{\theta_2}\right) \quad \text{for } X > 0,\ Y \to \infty. \tag{18d}$$

In addition, upon using $k_3 = -k_4$, the [3, 4] soliton is by design aligned to lie parallel to the Y-axis

$$K_{[3,4]} \approx A_{136}\,\mathrm{e}^{\theta_1+\theta_6}\left(\mathrm{e}^{\theta_3} + \frac{A_{146}}{A_{136}}\mathrm{e}^{\theta_4}\right) = A_{136}\,\mathrm{e}^{\theta_1+\theta_6}\left(\mathrm{e}^{\theta_3} + \mathrm{e}^{\theta_4}\right), \tag{18e}$$

in which we have already used that $b = 1$, such that $A_{136} = A_{146}$. Hence, in the far field, the solution $u(X, Y, \tau)$ is approximated by solitons whose centrelines are determined by the vanishing argument of the soliton solution (see (18) and referring to [13] for further details). Again using the above trio of skew symmetries, these centrelines are given by

$$[1,2]^- : \quad -(k_6-k_5)X + (k_6^2-k_5^2)Y + (k_6^3-k_5^3)\tau - \ln A_{235}/A_{135} = 0 \quad \text{for } X<0,\ Y\to-\infty \tag{19a}$$

$$[1,2]^+ : \quad -(k_6-k_5)X + (k_6^2-k_5^2)Y + (k_6^3-k_5^3)\tau - \ln A_{246}/A_{146} = 0 \quad \text{for } X>0,\ Y\to\infty \tag{19b}$$

$$[5,6]^- : \quad (k_5-k_6)X + (k_5^2-k_6^2)Y - (k_5^3-k_6^3)\tau - \ln A_{136}/A_{135} = 0 \quad \text{for } X<0,\ Y\to\infty \tag{19c}$$

$$[5,6]^+ : \quad (k_5-k_6)X + (k_5^2-k_6^2)Y - (k_5^3-k_6^3)\tau - \ln A_{246}/A_{245} = 0 \quad \text{for } X>0,\ Y\to-\infty \tag{19d}$$

$$[3,4] : \quad (k_3-k_4)X - (k_3^3-k_4^3)\tau = 0 \Longrightarrow X = k_4^2\tau. \tag{19e}$$

Figure 1 shows a top view of the five centrelines at three different times. The mean of the centrelines $[1,2]^-$ and $[5,6]^-$, as well as the offset $[1,2]^+$ and $[5,6]^+$ centrelines define the same centreline position by adding these line definitions, yielding

$$Y^* = \frac{1}{2}\frac{\ln\left(A_{235}/A_{136}\right)}{k_6^2-k_5^2} = \frac{1}{2}\frac{\ln\left(A_{245}/A_{146}\right)}{k_6^2-k_5^2} = \frac{\ln\left(\frac{2ak_5(k_5^2-k_4^2)}{2ck_6(k_6^2-k_4^2)}\right)}{2\left(k_6^2-k_5^2\right)}, \tag{20}$$

since $A_{245} = bA_{235}$ and $A_{146} = bA_{136}$ from (17), for which we are not per se required to choose $b = 1$.

Given the pairings of the A_{ijk} in (17), the function K in (14) can be rewritten more concisely as

$$\begin{aligned} K(X,Y,\tau) = {} & A_{135}\,\mathrm{e}^{(k_4^2+k_5^2+k_6^2)Y}\left(\mathrm{e}^{(k_5-k_4-k_6)X+(k_4^3+k_6^3-k_5^3)\tau}\right. \\ & \left. + a\,b\,c\;\mathrm{e}^{(k_4+k_6-k_5)X+(k_5^3-k_4^3-k_6^3)\tau}\right) \\ & + A_{235}\,\mathrm{e}^{(2k_5^2+k_4^2)Y}\left(\mathrm{e}^{-k_4X+k_4^3\tau} + b\,\mathrm{e}^{k_4X-k_4^3\tau}\right) \\ & + A_{136}\,\mathrm{e}^{(2k_6^2+k_4^2)Y}\left(\mathrm{e}^{-k_4X+k_4^3\tau} + b\,\mathrm{e}^{k_4X-k_4^3\tau}\right) \\ & + A_{236}\,\mathrm{e}^{(k_5^2+k_4^2+k_6^2)Y}\left(\mathrm{e}^{(k_6-k_5-k_4)X+(k_4^3+k_5^3-k_6^3)\tau}\right. \\ & \left. + \frac{b}{a\,c}\,\mathrm{e}^{(k_4+k_5-k_6)X+(k_6^3-k_4^3-k_5^3)\tau}\right). \end{aligned} \tag{21}$$

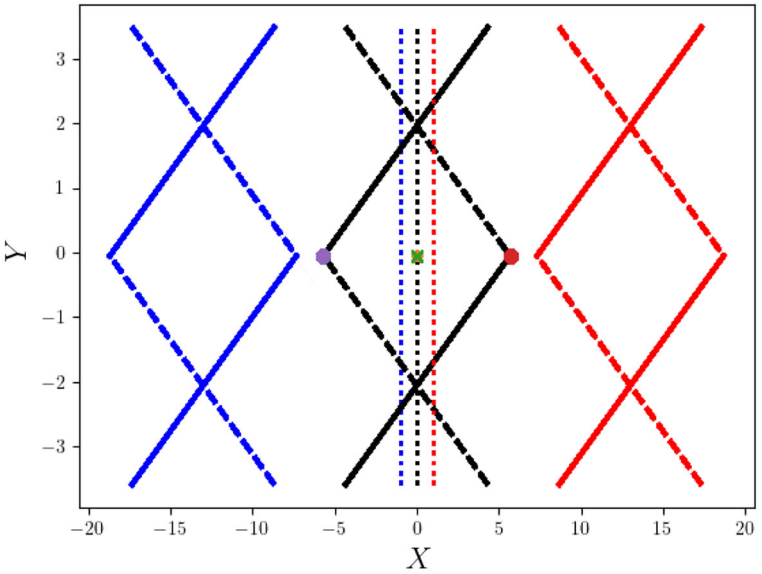

Fig. 1 Limiting the five centrelines of the three far-field solitons at three times leads to a candidate location of the maximum in space-time (X, Y, τ). Blue lines: $\tau < \tau^*$, black lines: $\tau = \tau^*$, red lines $\tau > \tau^*$. The slanted solid/dashed lines are the [1, 2] and [5, 6] solitons, respectively, and the vertical dotted lines are the [3, 4] soliton. The hypothesized maximum is asterisked at time τ^* when and where the black dotted line coincides with the centre of the black diamond. When $\tau = \tau^*$, the edges of the diamond coincide with Y^* as well as the centre of the diamond and are indicated by the dots; at time τ^*, the centre of the diamond coincides with the X-location of the [3, 4]-dotted line

Using (20) and (17), we find that

$$A_{235} = A_{136}\, \mathrm{e}^{2(k_6^2 - k_5^2)Y^*}, \tag{22}$$

using which (21) can be developed further by assigning $b = 1$ and defining $\mathrm{e}^{-\alpha} \equiv \sqrt{(ac)}$. We then find

$$\begin{aligned} K(X, Y, \tau) &= 2\mathrm{e}^{(k_4^2+k_5^2+k_6^2)Y} \\ &\times \Big(A_{135}\, \mathrm{e}^{-\alpha} \cosh\Big((k_5 - k_4 - k_6)X + (k_4^3 + k_6^3 - k_5^3)\tau + \alpha \Big) \\ &+ 2A_{136}\, \mathrm{e}^{(k_6^2 - k_5^2)Y^*} \cosh\left(k_4 X - k_4^3 \tau\right) \cosh\Big((k_6^2 - k_5^2)(Y - Y^*) \Big) \\ &+ A_{236}\, \mathrm{e}^{\alpha} \cosh\Big((k_6 - k_5 - k_4)X + (k_4^3 + k_5^3 - k_6^3)\tau - \alpha \Big) \Big), \end{aligned} \tag{23}$$

cf. the limiting case $a = b = c = 1$ in [13, eqns (50,51)]. Hence, K, K_X and K_{XX} are readily found and seen to be proportional to $\mathrm{e}^{(k_4^2+k_5^2+k_6^2)Y}$, whence (9), when rewritten as

$$u(X, Y, \tau) = 2(K K_{XX} - K_X^2)/K^2, \tag{24}$$

contains only even functions

$$1, \quad \cosh\Big((k_6^2 - k_5^2)(Y - Y^*)\Big) \quad \text{and} \quad \cosh^2\Big((k_6^2 - k_5^2)(Y - Y^*)\Big)$$

of $Y - Y^*$, so that u is symmetric about $Y = Y^*$, on which its maximum must lie.

3.2 Geometric Determination of Candidate Maximum

When the five centrelines given in (19) are plotted in Fig. 1 as functions of time, with the quadrant lines halted at $Y = Y^*$ for the three cases (of τ; see Fig. 1 caption), the candidate maximum is hypothesized to reside at the intersection of the middle of the black diamond and the black dotted [3, 4] line. Based on this geometric setting, the general expressions for the arguments (X^*, Y^*, τ^*) for the case $b = 1$ can be derived as

$$Y^* = \frac{1}{2}\ln\left(A_{245}/A_{146}\right)/(k_6^2 - k_5^2) = \frac{1}{2}\ln\left(A_{235}/A_{136}\right)/(k_6^2 - k_5^2), \tag{25a}$$

$$\begin{aligned}\tau^* &= \frac{1}{2}\ln\left(\frac{A_{136}A_{246}}{A_{135}A_{146}}\right)/(k_6^3 - k_5^3 - k_6k_4^2 + k_5k_4^2)\\ &= \frac{1}{2}\ln(ac)/(k_6^3 - k_5^3 - k_6k_4^2 + k_5k_4^2),\end{aligned} \tag{25b}$$

$$X^* = k_4^2\tau^*. \tag{25c}$$

When $a = b = c = 1$ (the case considered in [13]), (17) confirms that the argument $ac = A_{136}A_{246}/A_{135}A_{146}$ is equal to unity, whence $\tau^* = 0 = X^*$.

Given this geometric determination of the space-time point of maximum-wave amplification, in what follows the maximum of $U(X, \tau) \equiv u(X, Y^*, \tau)$ at (25) will be considered. It can be shown both numerically and analytically—solely using $b = 1$, $X = k_4^2\tau$, and $Y = Y^*$—that the candidate maximum point is a stationary point with $U_X = U_\tau = 0$. Details of the partially numerical evaluations will follow after first analysing how Y^* and τ^* behave when $\delta \to 0$.

To explore the Y^*-dependency on parameters a, b, c in (20), we consider the following cases:

(i) Choose $a = c = 1$ as in [13]: in the limit $k_5 - k_4 = \delta\sqrt{\tilde{A}} \to 0$ (see (15)), while $\tau^* = 0$ remains finite, the value of Y_* diverges as follows:

$$Y^* = \frac{1}{2(k_6^2 - k_5^2)}\ln\left(\frac{\delta\sqrt{\tilde{A}}\,k_5(k_5 + k_4)}{k_6(k_6^2 - k_4^2)}\right) \xrightarrow[\delta\to 0]{} -\infty. \tag{26a}$$

(ii) It is possible to choose appropriate values of a and c that remove the divergent singularity in (i) as $\delta \to 0$ by noting that $k_5 - k_4 = \delta\sqrt{\tilde{A}}$. Since

$$Y^* = \frac{1}{2}\frac{1}{k_6^2 - k_5^2}\ln\left(\frac{ak_5(k_5 - k_4)(k_5 + k_4)}{ck_6(k_6^2 - k_4^2)}\right)$$

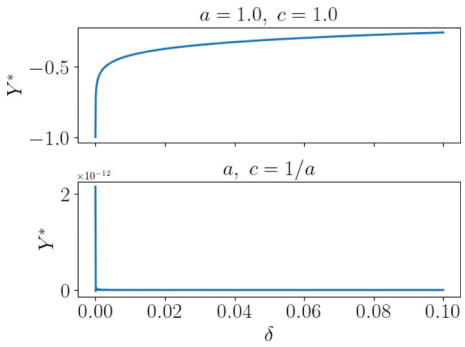

Fig. 2 Location Y^* of maximum amplification as a function of δ, for cases (i, ii) with $b = 1$ and $\delta = 10^{-7}$

$$= \frac{1}{2}\frac{1}{k_6^2 - k_5^2} \ln\left(\frac{a\delta\sqrt{\tilde{A}}}{c}\frac{k_5(k_5+k_4)}{k_6(k_6^2-k_4^2)}\right)$$

$$\tau^* = \frac{1}{2}\frac{\ln(ac)}{(k_6^3 - k_5^3 - k_6k_4^2 + k_5k_4^2)}, \tag{26b}$$

it follows that $\tau^* = 0$ when $ac = 1$ and $Y^* = 0$ when we furthermore take:

$$a = \sqrt{\frac{k_6(k_6^2 - k_4^2)}{\delta\sqrt{\tilde{A}}\,k_5(k_5+k_4)}} \quad \text{and} \quad c = \frac{1}{a} = \sqrt{\frac{\delta\sqrt{\tilde{A}}\,k_5(k_5+k_4)}{k_6(k_6^2-k_4^2)}}. \tag{26c}$$

Despite the fact that a diverges when $\delta \to 0$, the relevant coefficients in $K(X, Y, \tau)$ in (23) remain finite in the limit $\delta \to 0$, as seen from

$$A_{135} = -k_4k_5^2 - k_5k_4^2 + k_6k_5^2 - k_6k_4^2 + k_5k_6^2 + k_4k_6^2 \underset{\delta\to 0}{\longrightarrow} 4\tilde{A}\sqrt{\tilde{A}/2}, \tag{27a}$$

$$A_{235} = 2\,a\,k_5(k_5^2 - k_4^2) \underset{\delta\to 0}{\longrightarrow} 0, \tag{27b}$$

$$A_{136} = 2\,c\,k_6(k_6^2 - k_4^2) \underset{\delta\to 0}{\longrightarrow} 0, \tag{27c}$$

$$A_{236} = a\,c\,(-k_4k_6^2 - k_6k_4^2 + k_5k_6^2 - k_5k_4^2 + k_6k_5^2 + k_4k_5^2) \underset{\delta\to 0}{\longrightarrow} -A_{135}$$

$$= -4\tilde{A}\sqrt{\tilde{A}/2}. \tag{27d}$$

A plot of the Y^*-location for the two cases above can be seen in Fig. 2, where the divergence of Y^* as $\delta \to 0$ is clearly demonstrated when $a = c = 1$.

3.3 Computer-Algebra Analysis of Maximum Amplitude

Using (20) to fix $Y = Y^*$ (which is independent of b), we seek values of X^* and τ^* that yield stationary points of u in (24). Equivalently, $u_X(X^*, Y^*, \tau^*) = 0$ and

$u_\tau(X^*, Y^*, \tau^*) = 0$ are to be solved for X^* and τ^*. Since the denominators of both u_X and u_τ are non-zero, it suffices to determine the roots of their numerators, yielding

$$\hat{K}^2\hat{K}_{XXX} - 3\hat{K}\hat{K}_X\hat{K}_{XX} + 2\hat{K}_X^3 = 0 \tag{28a}$$

and

$$\hat{K}^2\hat{K}_{XX\tau} - \hat{K}\hat{K}_\tau\hat{K}_{XX} - 2\hat{K}\hat{K}_X\hat{K}_{X\tau} + 2\hat{K}_\tau\hat{K}_X^2 = 0, \tag{28b}$$

in which $\hat{K} \equiv K(X, Y^*, \tau)$. Using the skew symmetry $k_j = -k_{7-j}$ for $j = 1 \ldots 6$, we have

$$\begin{aligned}\hat{K} = 2&\left(b\,\mathrm{e}^{k_4(X-k_4^2\tau)} + \mathrm{e}^{-k_4(X-k_4^2\tau)}\right)\left(a\sigma_1 k_5\left(k_5^2 - k_4^2\right) + c\sigma_2 k_6\left(k_6^2 - k_4^2\right)\right)\\ &+ (k_5 + k_6)\,\sigma_3\Big(\,(k_6 + k_4)\,(k_5 - k_4)\left(b\,\mathrm{e}^{\alpha_{ppm}X - \gamma_{ppm}\tau} + ac\,\mathrm{e}^{-\alpha_{ppm}X + \gamma_{ppm}\tau}\right)\\ &+ (k_6 - k_4)\,(k_5 + k_4)\left(abc\,\mathrm{e}^{\alpha_{pmp}X - \gamma_{pmp}\tau} + \mathrm{e}^{-\alpha_{pmp}X + \gamma_{pmp}\tau}\right)\Big),\end{aligned} \tag{29}$$

in which

$$\alpha_{pmp} = k_4 - k_5 + k_6, \quad \alpha_{ppm} = k_4 + k_5 - k_6, \tag{30a}$$

$$\gamma_{pmp} = k_4^3 - k_5^3 + k_6^3, \quad \gamma_{ppm} = k_4^3 + k_5^3 - k_6^3 \tag{30b}$$

$$\sigma_1 = \mathrm{e}^{(k_4^2 + 2k_5^2)Y^*}, \quad \sigma_2 = \mathrm{e}^{(k_4^2 + 2k_6^2)Y^*} \quad \text{and} \quad \sigma_3 = \sqrt{\sigma_1\sigma_2}. \tag{30c}$$

Note that the first bracket in (29) is simply $2\cosh\left(k_4(X - k_4^2\tau)\right)$ when $b = 1$, which is constant when $X = k_4^2\tau$. If, in addition to $b = 1$, we set $ac = 1$, the exponential pairs in the second and third lines of (29) also collapse into single cosh terms.

Insertion of (29) into (28a) and (28b) is conducted within the `Maple` computer-algebra environment, whose cumbersome manipulations are not presented here. The substitution $X = k_4^2\tau$ in (28a) and (28b) admits progress through substantial algebraic expressions in which τ appears only as an exponential argument, whose consistent scaling invites the substitution

$$\beta \equiv \mathrm{e}^{(k_5 - k_6)(k_4^2 - k_5^2 - k_5k_6 - k_6^2)\tau}, \tag{31}$$

using which both (28a) and (28b) become sixth-order polynomials in β. Unfortunately, these sextics do not appear to be solvable for β for general a, b, c, but, when $b = 1$, it can be shown using `Maple` that U_X in (28a) factorises into the product of quadratic and quartic polynomials in β, the former yielding $\beta = \pm\sqrt{ac}$. Hence, using the positive root consistent with (31), when $b = 1$, an explicit solution of (28a) is

$$\tau^* = \frac{\ln(ac)}{2(k_5 - k_6)(k_4^2 - k_5^2 - k_5k_6 - k_6^2)} \quad \text{and} \quad X^* = k_4^2\tau^*, \tag{32}$$

and it transpires that this pair also solves (28b). If additionally $ac = 1$, it follows that $X^* = \tau^* = 0$ (cf. "case (ii)" above). That is, (20) and (32) together give *one* turning point of u, i.e., $\nabla u(X^*, Y^*, \tau^*) = 0$, though without being able to find the roots β of the above-mentioned quartic polynomial, we may be missing other such points, even when $b \neq 1$. We note that (32) is equivalent to the pair (25b) and (25c) when $b = 1$, thereby corroborating the above geometric argument. It is possible to make progress asymptotically when $b \approx 1$, but in this case even the leading-order perturbation to ac in the numerator of (32) is an unenlightening cumbersome combination of all parameters so far defined.

To confirm that $u(X^*, Y^*, \tau^*)$ is a maximum, we additionally invoke the principal-minors theorem (PMT) [24, 25] to show both that $u_{XX} < 0$ and that the determinant of the Hessian satisfies

$$H(u) \equiv u_{XX}u_{\tau\tau} - u_{X\tau}u_{\tau X} = u_{XX}u_{\tau\tau} - u_{X\tau}^2 > 0, \tag{33}$$

in which

$$\begin{aligned}
u_{XX} &= \big(2\,\hat{K}_{XXXX}\hat{K}^3 - (8\,\hat{K}_X\hat{K}_{XXX} + 6\,\hat{K}_{XX}^2)\hat{K}^2 \\
&\quad + 24\,\hat{K}\,\hat{K}_{XX}\hat{K}_X^2 - 12\,\hat{K}_X^4\big)/\hat{K}^4, && \text{(34a)}\\
u_{X\tau} &= \big(2\,\hat{K}_{XXX\tau}\hat{K}^3 - (2\,\hat{K}_\tau\hat{K}_{XXX} + 6\,\hat{K}_X\hat{K}_{XX\tau} + 6\,\hat{K}_{X\tau}\hat{K}_{XX})\hat{K}^2 \\
&\quad + (12\,\hat{K}_\tau\hat{K}_X\hat{K}_{XX} + 12\,\hat{K}_X^2\hat{K}_{X\tau})\hat{K} - 12\,\hat{K}_\tau\hat{K}_X^3\big)/\hat{K}^4, && \text{(34b)}\\
u_{\tau\tau} &= \big(2\,\hat{K}_{XX\tau\tau}\hat{K}^3 - (4\,\hat{K}_\tau\hat{K}_{XX\tau} + 2\,\hat{K}_{\tau\tau}\hat{K}_{XX} + 4\,\hat{K}_X\hat{K}_{X\tau\tau} + 4\,\hat{K}_{X\tau}^2)\hat{K}^2 \\
&\quad + (4\,\hat{K}_\tau^2\hat{K}_{XX} + 16\,\hat{K}_\tau\hat{K}_X\hat{K}_{X\tau} + 4\,\hat{K}_{\tau\tau}\hat{K}_X^2)\hat{K} - 12\,\hat{K}_\tau^2\hat{K}_X^2\big)/\hat{K}^4. && \text{(34c)}
\end{aligned}$$

Asymptotic approximations of u_{XX} and $H(u)$ are non-trivial to determine due to the appearance of δ in both rational functions of surds and rational-function powers thereof. However, via judicious iterative substitutions in `Maple`, one can establish the following limiting forms:

$$\begin{aligned}
\frac{u_{XX}}{\tilde{A}^2} &= -81 + 176\sqrt{3}\sqrt[4]{2}\sqrt{\delta} - 436\sqrt{2}\delta + \mathcal{O}(\delta^{3/2}), \quad \delta \to 0 && \text{(35a)}\\
\frac{H(u)}{\tilde{A}^6} &= 5184\,(\sqrt{3}\sqrt[4]{2}\sqrt{\delta} - 6\sqrt{2}\delta) + \mathcal{O}(\delta^{3/2}), \quad \delta \to 0 && \text{(35b)}\\
\frac{u_{XX}}{\tilde{A}^2} &= -3 - \frac{9}{\delta^2} + \frac{1953}{32\,\delta^4} - \frac{639\sqrt{2}}{4\,\delta^5} + \mathcal{O}(\delta^{-6}), \quad \delta \to \infty && \text{(35c)}\\
\frac{H(u)}{\tilde{A}^6} &= 18\,\delta^4 + 72\sqrt{2}\delta^3 + 81\,\delta^2 - 324\sqrt{2}\delta + \mathcal{O}(1), \quad \delta \to \infty. && \text{(35d)}
\end{aligned}$$

Expressions (35) are compared in Fig. 3 against numerically computed values of u_{XX} and $H(u)$. The combination of these expressions and the numerics confirms that $-81\tilde{A}^2 < u_{XX} < -3\tilde{A}^2$ and $H(u) > 0$ for all $\delta, \tilde{A} > 0$, thereby satisfying the conditions of the PMT and proving that $u(X^*, Y^*, \tau^*)$ is indeed a maximum; this

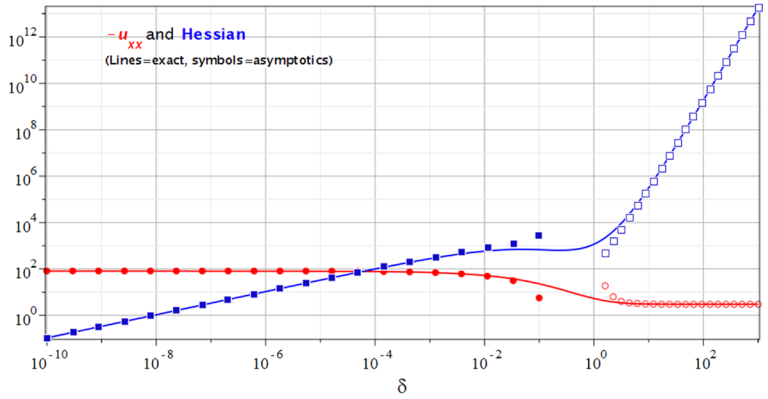

Fig. 3 Log–log plot showing comparison of numerically computed $-u_{XX}/\tilde{A}^2$ (red line) and $H(u)/\tilde{A}^6$ (blue line) with (higher order forms of) asymptotic approximations (35a) (red discs), (35b) (blue filled squares), (35c) (red circles), and (35d) (blue open squares). See text for discussion

finding is qualitatively independent of a and c. It remains only to show that it is the global maximum.

Using the starred coordinates, the maximum-amplification factor $u(X^*, Y^*, \tau^*)/\tilde{A}$ can be approximated asymptotically as $\delta \to 0$. When $ac = 1$, equivalently $\tau^* = 0$, the asymptotics are straightforward though mechanical. However, when $ac \neq 1$, (15) and (32) introduce exponentials of rational functions of δ, of which asymptotic approximation is far more subtle, but still negotiable. It transpires that the amplification factor is dependent upon only δ, the exact expression being

$$\frac{u(X^*, Y^*, \tau^*)}{\tilde{A}} = \frac{20\alpha_1\alpha_2 + \alpha_3}{(\alpha_1 + \alpha_4)^2}, \tag{36}$$

in which

$$\alpha_1 = \sqrt{\delta\,(3\sqrt{2} + 2\,\delta)(3\sqrt{2}\delta + \delta^2 + 4)(\sqrt{2} + 2\,\delta)(\sqrt{2} + \delta)}, \tag{37a}$$

$$\alpha_2 = \sqrt{2} + \frac{9\sqrt{2}\delta^2}{5} + \frac{17\,\delta}{5} + \frac{3\,\delta^3}{5}, \tag{37b}$$

$$\alpha_3 = \left(144\,\delta^5 + 824\,\delta^3 + 320\,\delta\right)\sqrt{2} + 24\,\delta^6 + 686\,\delta^4 + 1040\,\delta^2 + 72, \tag{37c}$$

$$\alpha_4 = 6\sqrt{2}\delta^2 + 2\,\delta^3 + 2\sqrt{2} + 10\,\delta, \tag{37d}$$

and of which the asymptotic approximation as $\delta \to 0$ is

$$9 - 8\sqrt{3}\sqrt[4]{2}\sqrt{\delta} + 16\sqrt{2}\delta - \frac{19\,2^{3/4}\sqrt{3}}{3}\delta^{3/2} + 8\,\delta^2 - \frac{23\sqrt{3}\sqrt[4]{2}}{72}\delta^{5/2} + \mathcal{O}(\delta^3). \tag{38}$$

Figure 4 compares the exact and approximate amplification factors, between which the difference is indiscernible on this scale as $\delta \to 0$, at which limit a non-logarithmic

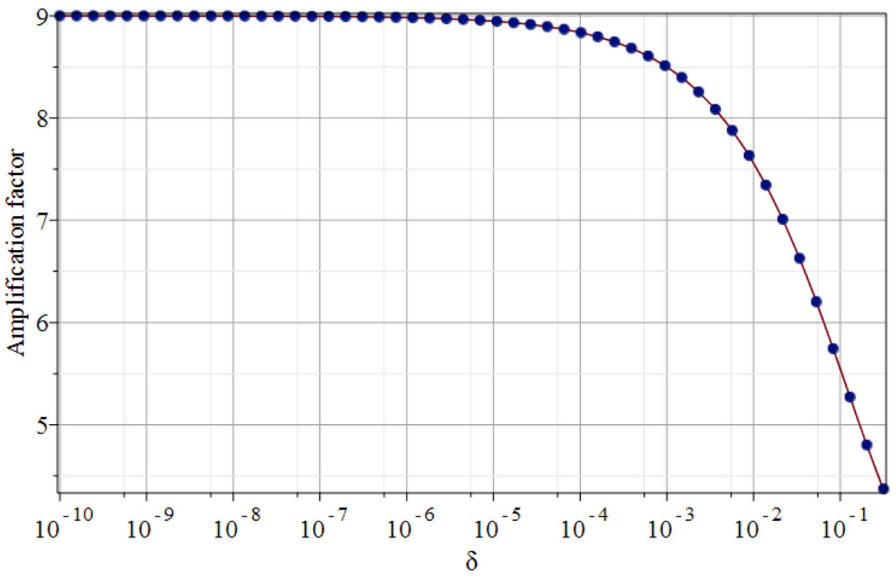

Fig. 4 Semilog plot of amplification factor, as a function of δ, given by exact formula (36) (red line) and its asymptotic approximation (38) (blue discs). These curves all have $b = 1$ and are independent of a, c and $\tilde{A}$. Larger values of δ (e.g., $\delta > 0.1$) are accommodated to illustrate the range of validity of the asymptotic result

replot (not presented) of Fig. 4 shows cusped behaviour, completing the proof that $u(X^*, Y^*, \tau^*)/\tilde{A}$ is the unique maximum, and that it is independent of a, c, and $\tilde{A}$. Independent computations conducted in Python fully corroborate numerically all theoretical results derived in this section.

4 Numerical Modelling

Both the Benney–Luke equations (BLE) and potential-flow equations (PFE) are approximated in space and time by discretisation of their respective variational principles (VPs). We need a numerical approach with a suitable computational domain given that the interactions of two and three solitons of equal far-field amplitudes are defined on an infinite horizontal plane. We denote these two- and three-solution interactions and simulations by SP2 and SP3 respectively, with details of two-soliton solutions SP2 defined in [13]. One approximation is to consider a domain periodic in the x-direction and, given the y-symmetry of the solutions, a channel with walls in the y-direction instead of an infinite domain. However, when we plot the two-soliton and three-soliton solutions for η, Φ or ϕ and the three velocity components (u_1, u_2, u_3), we note that ϕ and Φ are not periodic in x; see Figs. 14 and 5. To resolve this issue, we partition the velocity potential in each of cases SP2 and SP3 into a background part and an x-periodic perturbation. For the PFE, the partition is

$$\phi(x, y, z, t) = U_0(y, z)x + \tilde{\phi}(x, y, z, t), \tag{39}$$

with a (y, z)-dependent static function $U_0(y, z)$, and, similarly, for the BLE the partition is

$$\Phi(x, y, t) = U_0(y)x + \tilde{\Phi}(x, y, t), \tag{40}$$

wherein the variables are scaled according to (2), but, for simplicity, the hats are generally (unless confusion arises) dropped in (40) and hereafter.

The original and partitioned VPs for the PFE are respectively

$$0 = \delta \int_0^T \iint_{\Omega_h} \int_0^{h(x,y,t)} \partial_t \phi + \frac{1}{2}|\nabla\phi|^2 + g(z - H_0)\,\mathrm{d}z\,\mathrm{d}x\,\mathrm{d}y\,\mathrm{d}t \tag{41a}$$

$$0 = \delta \int_0^T \iint_{\Omega_h} \int_0^{h(x,y,t)} \partial_t \tilde{\phi} + \frac{1}{2}(U_0 + \partial_x\tilde{\phi})^2 + \frac{1}{2}\left(x\partial_y U_0 + \partial_y\tilde{\phi}\right)^2 + \frac{1}{2}\left(x\partial_z U_0 + \partial_z\tilde{\phi}\right)^2 + g(z - H_0)\,\mathrm{d}z\,\mathrm{d}x\,\mathrm{d}y\,\mathrm{d}t, \tag{41b}$$

both of which are defined on $\Omega_h = \{(x, y) \in [x_1, x_2] \times [y_1, y_2]\}$ for appropriately chosen values of x_1, x_2, y_1 and y_2 that render the perturbed velocity potential x-periodic. The original and partitioned VPs for the BLE are respectively

$$0 = \delta \int_0^T \iint_{\Omega_h} \eta\partial_t\Phi - \Phi\partial_t\eta + \frac{\mu}{2}\nabla\eta\cdot\nabla\partial_t\Phi - \frac{\mu}{2}\nabla\Phi\cdot\nabla\partial_t\eta + \frac{1}{2}(1 + \epsilon\eta)|\nabla\Phi|^2 + \frac{1}{2}\eta^2 + \mu\left(\nabla q\cdot\nabla\Phi - \frac{3}{4}q^2\right)\mathrm{d}x\,\mathrm{d}y\,\mathrm{d}t \tag{42a}$$

$$0 = \delta \int_0^T \iint_{\Omega_h} \eta\partial_t\tilde{\Phi} - \tilde{\Phi}\partial_t\eta + \frac{\mu}{2}\nabla\eta\cdot\nabla\partial_t\tilde{\Phi} - \frac{\mu}{2}\nabla\tilde{\Phi}\cdot\nabla\partial_t\eta + \frac{1}{2}(1 + \epsilon\eta)|\nabla(U_0x + \tilde{\Phi})|^2 + \frac{1}{2}\eta^2 + \mu\left(\nabla q\cdot\nabla(U_0x + \tilde{\Phi}) - \frac{3}{4}q^2\right)\mathrm{d}x\,\mathrm{d}y\,\mathrm{d}t. \tag{42b}$$

Using the above VP (42b), or the partitioning (40) with the BLE (5), the reformulated equations for $\{\eta, \tilde{\Phi}\}$ become

$$\partial_t\tilde{\Phi} - \frac{\mu}{2}\partial_t\nabla^2\tilde{\Phi} + \frac{\epsilon}{2}\left|\nabla(U_0x + \tilde{\Phi})\right|^2 + \eta = 0, \tag{43a}$$

$$\partial_t\eta - \frac{\mu}{2}\partial_t\nabla^2\eta + \nabla\cdot\left\{(1 + \epsilon\eta)\,\nabla(U_0x + \tilde{\Phi})\right\} - \frac{2\mu}{3}\nabla^4(U_0x + \tilde{\Phi}) = 0. \tag{43b}$$

The numerical models comprise discretisations of time-discrete versions, of the two partitioned VPs above, within the finite-element environment *Firedrake* [15], in which

the VP for the PFE is first transformed to a fixed domain. The spatial discretisation for the PFE can be varied separately in the horizontal and (transformed) vertical directions using a vertically extruded mesh by either varying the (quadrilateral or line) elements and/or varying the Gauss–Lobatto–Legendre (GLL) polynomial order. We denote the polynomials of order n_h (horizontal) and n_v (vertical) by CGn_h or CGn_v, respectively, the notation CG reflecting the Continuous Galerkin approach: the lowest orders used are CG2 in both horizontal and vertical (with $n_h = n_v = 2$). The respective weak formulations are subsequently generated automatically within Firedrake using the "functional" command derivative (see 17.5.1 in [26] and 6.4 in [27]). This approach yields the functional derivatives analytically—without using the divergence theorem—such that the first-order derivatives in the VPs are preserved, acting on the velocity potential and/or its test function, the latter equivalent to the variational derivatives $\delta\Phi$, $\delta\eta$, δq or $\delta\phi$, δh. This entirely variational-based procedure reduces both development time and the introduction of human error given that, for the PFE, the weak formulations are algebraically much more cumbersome than for the basic VP as a result of both explicit mesh motion and implicit mesh "motion" induced by the coordinate transformations that render static the fixed computational domain. The time-discrete VPs and further details on the coordinate transformation are relegated to Appendix C.

4.1 Periodisation of Soliton Dynamics

We have shown that the BLE (5) and PFE (1) require modification[3] to accommodate simulation in the proposed x-periodic domain. The potential-flow velocity potential is therefore partitioned into a static, non-periodic part and a dynamic, periodic part. Consequently, the velocity-potential perturbations $\tilde{\phi}$ (in the PFE) and $\tilde{\Phi}$ (in the BLE) are by construction made periodic in the x-direction. We now describe how we impose initial conditions for η_0, $\tilde{\Phi}_0$ and $\tilde{\phi}_0$.

First, for the BLE, a function η_0 is defined by $\widehat{\eta}$ in (11a) evaluated at $\epsilon = 0$ as

$$\eta(x, y, t_0) \equiv \eta_0(x, y) = 2\Big(\frac{4}{3}\Big)^{1/3} \partial_{XX} \ln\big(K(X, Y, \tau_0)\big). \tag{44}$$

The moving three-line-soliton (SP3) solution and the interacting two-line soliton solution (SP2) investigated on an infinite plane, respectively, have an X-shaped and Y-shaped structure, which allows definition of a (nearly) periodic analogue for numerical simulation in an x-periodic domain. Snapshots of the SP3 solution, augmented with coordinate pairs (x_1, y_1), (x_2, y_1), (x_2, y_2) and (x_2, y_2) outlining the prospective periodic domains, are shown in Fig. 5.

Because, as $x \to \pm\infty$, the function η_0 returns to zero (as with sech-shaped soliton profiles), we can choose x_1, x_2, and y_2, such that $\eta_0(x_1, y_2) = \eta_0(x_2, y_2)$ and $\eta_{0x}(x_1, y_2) = 0 = \eta_{0x}(x_2, y_2)$ as in [13]. Using the η_0 defined on an infinite plane, the periodic variation η_0 thereof is defined as

[3] A factor ϵ was missing in (42b) of [13] but not in the code used.

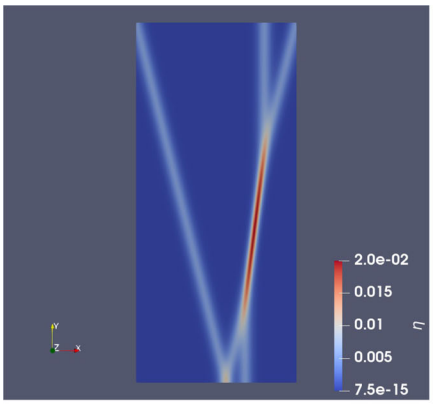

(a) η

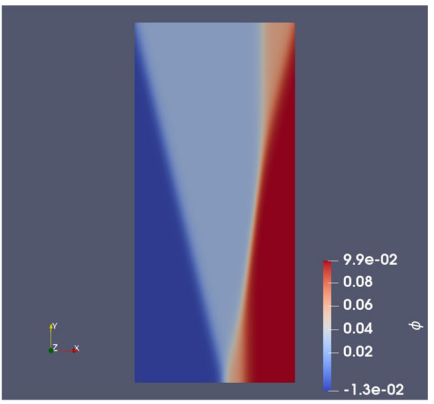

(b) ϕ at free surface

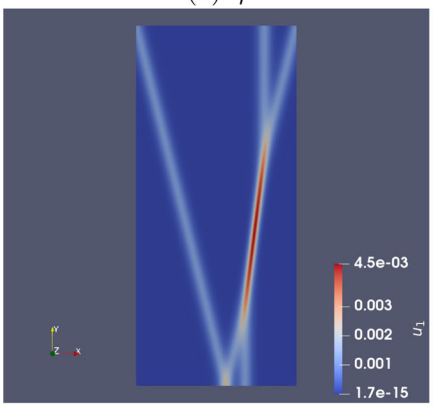

(c) u_1

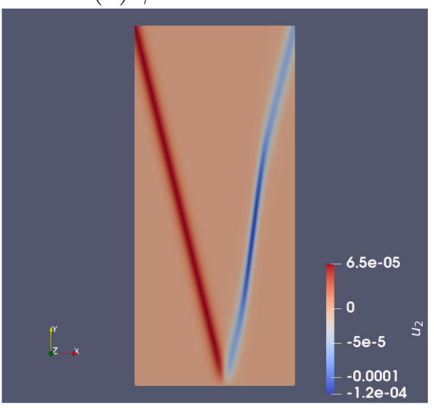

(d) u_2

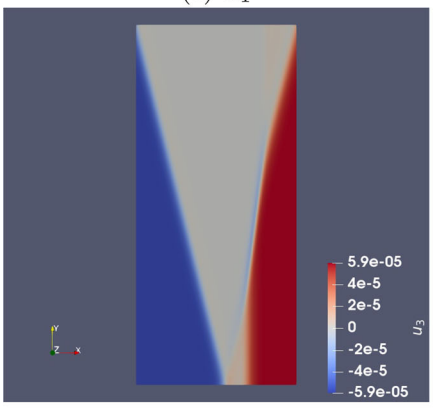

(e) u_3

Fig. 5 Top view of a sample initial condition and resulting velocity components for three-soliton interactions (SP3), calculated via (44) and (50) and shown at $\hat{t} = -200$ for $\epsilon = 0.05$, $\mu = \epsilon^2$, $H_0 = 20$ m

$$\eta_0\big(x + n(x_2 - x_1), y\big) = \eta_0(x, y), \tag{45}$$

where $x \in [x_1, x_2)$ and $n \in \mathbb{Z}$. Combining (10) and the velocity potential (11b), the velocity potential reads

$$\Phi_0(x, y, t_0) \equiv \Phi_0(x, y) = 2\sqrt{\epsilon}\left(\frac{4\sqrt{2}}{9}\right)^{1/3} \partial_X \ln\big(K(X, Y, \tau_0)\big). \tag{46}$$

Hence, we find that $\Phi_{0x}(x_1, y) = \eta_0(x_1, y) = \eta_0(x_2, y) = \Phi_{0x}(x_2, y)$, such that Φ_0 has a tanh-shaped profile in the x-direction. Consequently, $\Phi_0(x_1, y)$ and $\Phi_0(x_2, y)$ cannot be equal. We, therefore, require the function $U_0(y)$ in (40) to be such that $\tilde{\Phi}_0(x_1, y) = \tilde{\Phi}_0(x_2, y)$ becomes periodic or equivalently $\Phi_0(x_1, y) - U_0(y)x_1 = \Phi_0(x_2, y) - U_0(y)x_2$. Given this function and the previous two equations, we derive that

$$U_0(y) = \frac{\Phi_0(x_2, y) - \Phi_0(x_1, y)}{x_2 - x_1}. \tag{47a}$$

Consequently, the periodic initial condition for $\tilde{\Phi}$ may be defined by

$$\tilde{\Phi}_0\big(x + n(x_2 - x_1), y\big) = \Phi_0(x, y) - U_0(y)x, \tag{48}$$

where $x \in [x_1, x_2)$ and $n \in \mathbb{Z}$. Recall that the hats for coordinates in the BLE domain have been dropped, such that $x_{1,2}$, $y_{1,2}$ in BLE and PFE differ by scaling factors.

The procedure for the PFE is similar when it is undertaken with the $\phi(x, y, z, t_0) \equiv \phi_0(x, y, z)$ expression. To wit, the above procedure for BLE is thus replaced by

$$U_0(y, z) = \frac{\phi_0(x_2, y, z) - \phi_0(x_1, y, z)}{x_2 - x_1}, \tag{49a}$$

while using (11) up to $\mathcal{O}(\mu^2)$ or $\mathcal{O}(\mu^4)$. Consequently, the periodic initial condition for the velocity potential is defined by

$$\tilde{\phi}_0(x + n(x_2 - x_1), y, z) = \phi_0(x, y, z) - U_0(y, z)x, \tag{50}$$

where $x \in [x_1, x_2)$ and $n \in \mathbb{Z}$. The z-dependence of $\tilde{\phi}$ follows automatically by solving the (discretised) Laplace equation but in the (transformed) equations or variational principle the substitution $\phi(x, y, z, t) = U_0(y, z)x + \tilde{\phi}(x, y, z, t)$ is made. A difference with the approach for the BLE is that Φ is defined at the bottom $z = 0$, while for the PFE, the prognostic

$$\begin{aligned}\psi(x, y, t) &\equiv \phi(x, y, h(x, y, t), t)\\ &= U_0(y, h(x, y, t))x + \tilde{\phi}(x, y, h(x, y, t), t)\\ &= U_0(y, h(x, y, t))x + \tilde{\psi}(x, y, t)\end{aligned} \tag{51}$$

is defined at the free surface $z = h(x, y, t)$. Note that the functions $U_0(y)$ and $U_0(y, z)$ differ between BLE and PFE due to both the different scalings as well as the inclusion of higher order $\mathcal{O}(\mu)$, $\mathcal{O}(\mu^2)$ terms in $\Phi_0(x, y)$ and $\phi_0(x, y, z)$. Further details on the particular expressions for interacting solitons are provided in Appendix B.

5 Maximum Amplification of Three Interacting Solitons with Equal Far-Field Amplitudes

A series of numerical simulations of the three-soliton interactions have been undertaken with both the variational Benney–Luke and potential-flow discretisations. Each simulation uses a different nonlinearity or amplitude measure, $\epsilon = 0.01$ and/or 0.05, based on the scaling of the Benney–Luke equations (BLE). As initial conditions, we seed both sets of equations with the exact solutions of the Kadomtsev–Petviashvili equation (KPE) we have derived for three interacting line-solitons (denoted by KPE-SP3) at a time before the growth to the maximum occurs in space and time. The goal of the simulations is to assess what the maximum amplification can become in these more accurate or faithful Benney–Luke and potential-flow models of water-wave dynamics. For the exact KPE-SP3 solution used in this initialisation, we take $\delta = 10^{-5}, 10^{-10}$, for which the computations underlying Fig. 4 reveal an amplification factor of up to 8.9998, whose error relative to the ninefold theoretical maximum is $1.8 \times 10^{-3}\%$. First, simulations for the BLE are presented and, subsequently, simulations for the potential-flow equations (PFE); finally, a brief comparison between these simulations is undertaken. We emphasize that the use of variational space-time discretisations means that there is no loss in wave amplitude due to numerical artefacts.

5.1 Amplification in the Benney–Luke Equations

Table 1 shows the parameter values used for the BLE simulations; to highlight a few of them, we use a non-dimensional KPE-amplitude of $\tilde{A} \approx 0.4543$, yielding a BLE amplitude of $\widehat{A} = 0.5$, for each of the nonlinearity parameters $\epsilon = 0.01$ and 0.05.

Table 1 Solution and numerical parameter values employed in the simulations of the BLE for the three-soliton interactions (BLE-SP3)

$\tilde{A}$		δ	k_4	k_5	k_6	a	b	c
$\frac{1}{2}\left(\frac{3}{4}\right)^{1/3}$		10^{-10}	0.4766	0.4766	1.4298	2.9129×10^5	1	$1/a$
ϵ	μ	$L_{\widehat{x}}$	$L_{\widehat{y}}$	$\widehat{T}$	$N_{\widehat{x}}$	$N_{\widehat{y}}$	$\Delta\widehat{x} = \frac{L_{\widehat{x}}}{N_{\widehat{x}}}$	$\Delta\widehat{y} = \frac{L_{\widehat{y}}}{N_{\widehat{y}}}$	$\Delta\widehat{t}$
0.01	ϵ^2	10.3722	25	140	166	400	0.0625	0.0625	0.005
0.05	ϵ^2	28.6701	30	80	230	240	0.125	0.125	0.005

The values of parameters k_i are calculated from (15). Here, $\widehat{T}$ is the total simulation time defined as $\widehat{T} = \widehat{t}_{\text{end}} - \widehat{t}_0$, and $L_{\widehat{x}} = \widehat{x}_2 - \widehat{x}_1$, so $\Delta\widehat{x} \approx \Delta\widehat{y}$ given that the structure of the fields is quite evenly spaced in the horizontal directions. Basis function CG4 was used

The respective simulations run in the time intervals $[-110, 30]$ (for $\epsilon = 0.01$) and in $[-60, 20]$ (for $\epsilon = 0.05$), and have been undertaken on Leeds arc4-HPC on (typically) 40 cores, requiring, respectively, 919 minutes and 1764 minutes to run. The time step was chosen by trial and error to obtain a stable simulation, as judged by monitoring the energy evolution over time. GLL basis functions CG4 were used, yielding formal fifth-order (spectral) spatial accuracy. A second-order Störmer–Verlet (SV) time-stepping scheme was chosen.

The initial conditions for η and Φ for the BLE simulations with $\epsilon = 0.01$ (at time $t = -110$) and $\epsilon = 0.05$ (at time $t = -60$) are shown in Fig. 6. The initial times were chosen, such that they are prior to the time when the maximum in the exact KPE solution starts to grow from $4\tilde{A}$, caused by the pair of two-soliton interactions to its KPE maximum of nearly $9\tilde{A}$.

A pair of solution snapshots for the BLE simulation with $\epsilon = 0.01$ is shown in Fig. 7, together with cross-sections at $\hat{y} = 24$ at BLE times $\{-30, 0\}$. These results give impressions of the overall solution fields including the minor oscillations of small-scale travelling waves shed off the main three solitons. Further results for this BLE simulation in Fig. 8a show the maximum-wave amplitude in the domain in time. It has a maximum of nearly 4.5 around BLE time -50, whereafter the maximum slightly decreases and swings up. Figure 8b shows the far-field amplitude $\widehat{A} = \max_{\hat{x}} \widehat{\eta}$ at the location $\hat{y} = 24$, which reveals oscillations ranging from $\widehat{A} = 0.5$ to 0.56, the latter at the initial time, and then more or less settling around $\widehat{A} = 0.52 \pm 0.01$. Minor waves dispersing from the main three solitons lead to an increase of this local maximum relative to the $\tilde{A} = \frac{1}{2}(3/4)^{1/3} \approx 0.4543$ or $\widehat{A} = 0.5$. Figure 8c reveals that the maximum amplification $\max(\hat{\eta})/\widehat{A}$ over time reaches a maximum of circa 8.8, which thereafter settles to circa 8.2. Finally, Fig. 8d concerns the energy evolution over time relative to the initial energy. The energy deviations fluctuate around 10^{-4}. While initially a clear downward drift of energy is seen, when we simulate beyond time zero, the energy deviations turn upward, indicating that the oscillations settle on the longer time-scale of the "cnoidal" period of these soliton interactions, cf. the simulations in the accompanying supplementary movie for [13]. This monitoring of energy suggests that our simulations are stable.

To assess how an increase in wave amplitude affects these amplification results, we show a BLE simulation with $\epsilon = 0.05$ in the four-panel graphs of Fig. 9. The BLE simulation time interval is now $[-60, 20]$, different from the previous case with $\epsilon = 0.01$, because the changed values of ϵ and μ affect the time transformation, cf. (7), between BLE and KPE by a factor of circa 2.24, which is consistent with the ratio of times when the amplifications start to grow towards their maximum. The results remain largely similar, but oscillations due to smaller scale wave dispersion increase; see also Fig. 10. The maximum amplification lies within (7.6, 8.8). Notably, the energy deviations indicate numerical stability and remain around 10^{-4} except near the initial time at BLE time circa $\hat{t} = -60$. In both simulations, there seems an initial small adjustment of the energy near to or at the initial time. Discussion regarding the information gleaned from these simulations is deferred until Sect. 6.

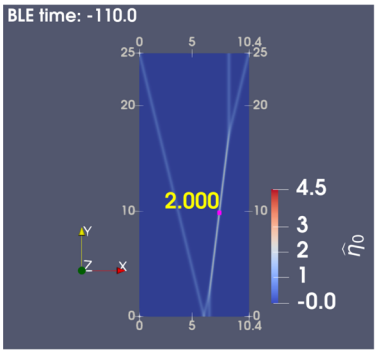

(a) Initial condition $\widehat{\eta}_0$ for $\epsilon = 0.01$

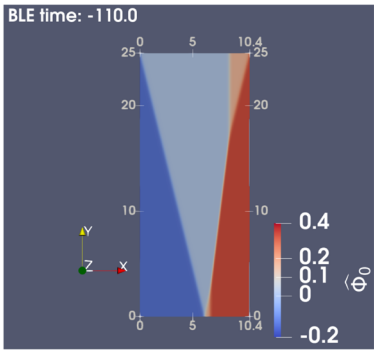

(b) Initial condition $\widehat{\phi}_0$ for $\epsilon = 0.01$

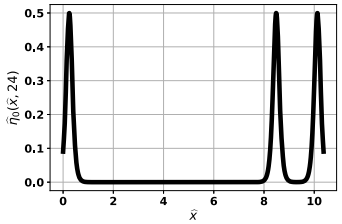

(c) $\widehat{\eta}_0(\widehat{x}, 24)$ for $\epsilon = 0.01$

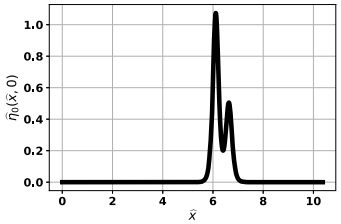

(d) $\widehat{\eta}_0(\widehat{x}, 0)$ for $\epsilon = 0.01$

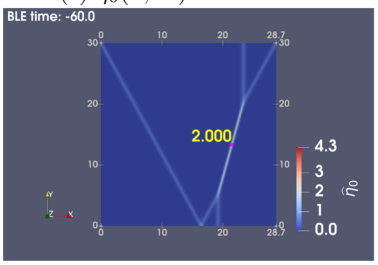

(e) Initial condition $\widehat{\eta}_0$ for $\epsilon = 0.05$

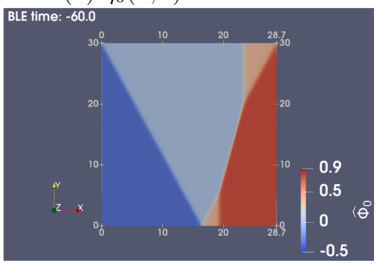

(f) Initial condition $\widehat{\Phi}_0$ for $\epsilon = 0.05$

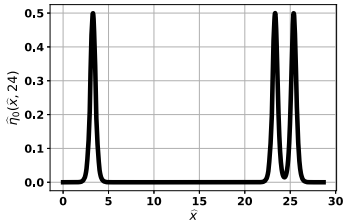

(g) $\widehat{\eta}_0(\widehat{x}, 24)$ for $\epsilon = 0.05$

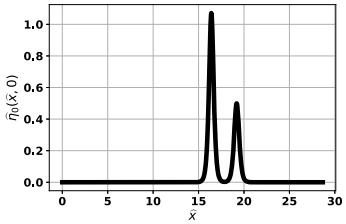

(h) $\widehat{\eta}_0(\widehat{x}, 0)$ for $\epsilon = 0.05$

Fig. 6 Initial conditions for BLE-SP3 simulation with $\epsilon = 0.01, 0.05$. (**a**, **e**) $\widehat{\eta}_0$ and (**b**, **f**) total $\widehat{\Phi}_0$, given at times $\widehat{t}_0 = -110$ (for $\epsilon = 0.01$) and $\widehat{t}_0 = -60$ (for $\epsilon = 0.05$), respectively. Panels (**c**, **d**) and (**g**, **h**) show cross-sections of $\widehat{\eta}_0$ at the far-field $\widehat{y} = 24$, and on the lower boundary $\widehat{y} = \widehat{y}_* = 0$, respectively

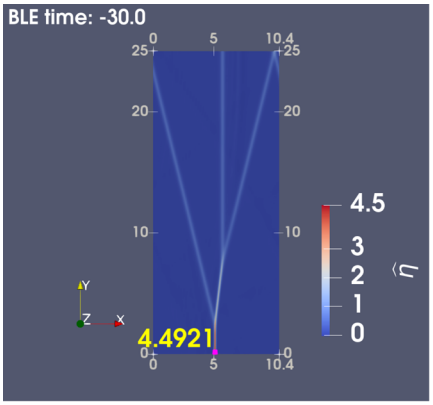

(a) $\widehat{\eta}$ at $\widehat{t} = -30$

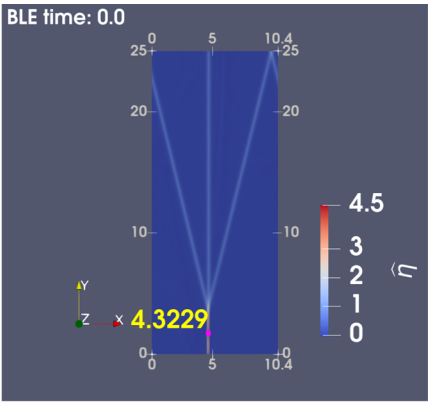

(b) $\widehat{\eta}$ at $\widehat{t} = 0$

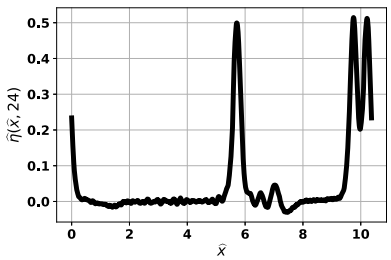

(c) $\widehat{\eta}(\widehat{x}, 24)$ at $\widehat{t} = -30$

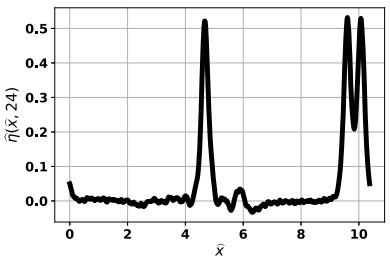

(d) $\widehat{\eta}(\widehat{x}, 24)$ at $\widehat{t} = 0$

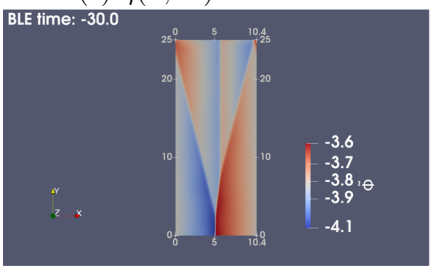

(e) $\tilde{\Phi}$ at $\widehat{t} = -30$

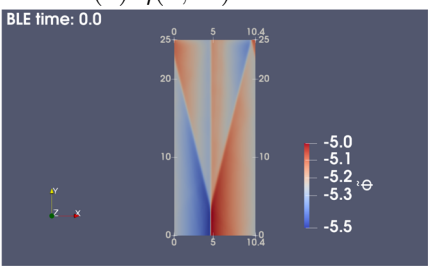

(f) $\tilde{\Phi}$ at $\widehat{t} = 0$

Fig. 7 Numerical three-soliton solution for the Benney–Luke equations (BLE-SP3) for $\epsilon = 0.01$ at times $\widehat{t} = -30$ (left-hand side panels) and $\widehat{t} = 0$ (right-hand side panels), respectively. Panels **a** and **b** show the surface elevation $\widehat{\eta}$ which is seen to attain a global maximum at $\widehat{t} = -30$. Panels **c** and **d** show that the height of $\widehat{\eta}$ in the far-field $\widehat{y} = 24$ is close to the initial height 0.5 at both times. Panels **e** and **f** show the potential $\tilde{\Phi}$

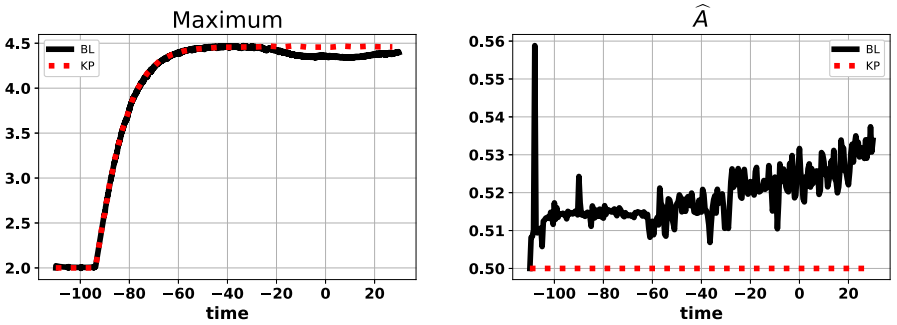

(a) Maximum values of $\widehat{\eta}$

(b) $\widehat{A}$ against time

(c) max/$\widehat{A}$ against time

(d) Deviation of energy

Fig. 8 Results obtained for a three-soliton simulation of the Benney–Luke equations (BLE-SP3) with $\epsilon = 0.01$, employing finite-element polynomials of order CG4. The red dashed line is computed from the rescaled KPE solution as a reference. Panels show: **a** maximum values of $\widehat{\eta}$ over time; **b** $\widehat{A} := \max_{\widehat{x}}(\widehat{\eta}(\cdot, \widehat{y} = 24, \widehat{t}))$; **c** amplification $\max(\widehat{\eta})/\widehat{A}$ against time; and **d** energy deviation $E(\widehat{t}) - E(\widehat{t_0})$ in time, where $E(\widehat{t})$ is defined in (6) for the BLE system and $\widehat{t_0} = -110$. The energy deviation from $E(\widehat{t_0}) = 9.227$ is of the order of 10^{-4}, suggesting that the numerics are stable

5.2 Amplification in the Potential-Flow Equations

Simulations of the PFE with the travelling Y-shaped soliton-complex of two interacting solitons of equal amplitude successfully show that the fourfold amplification in that complex can persist at about 3.85 to 4.05, albeit with some dispersive effects for $\epsilon = 0.05$ and $A \approx 0.416$ (not shown here, see [28] and Appendix B).

We therefore carry out simulations of the PFE using $\epsilon = 0.01$, seeded with the KPE three-soliton solution well prior to the KPE time $\tau = 0$ of maximum amplification, i.e., they are seeded at a time when the maximum amplification of the three far-field solitons at $A = 0.1$ m is found in two (local) maxima of $4A$. The solution around these two local maxima consists essentially of the travelling Y-shaped soliton. While each Y-complex is steady, they are travelling in different directions and their interaction

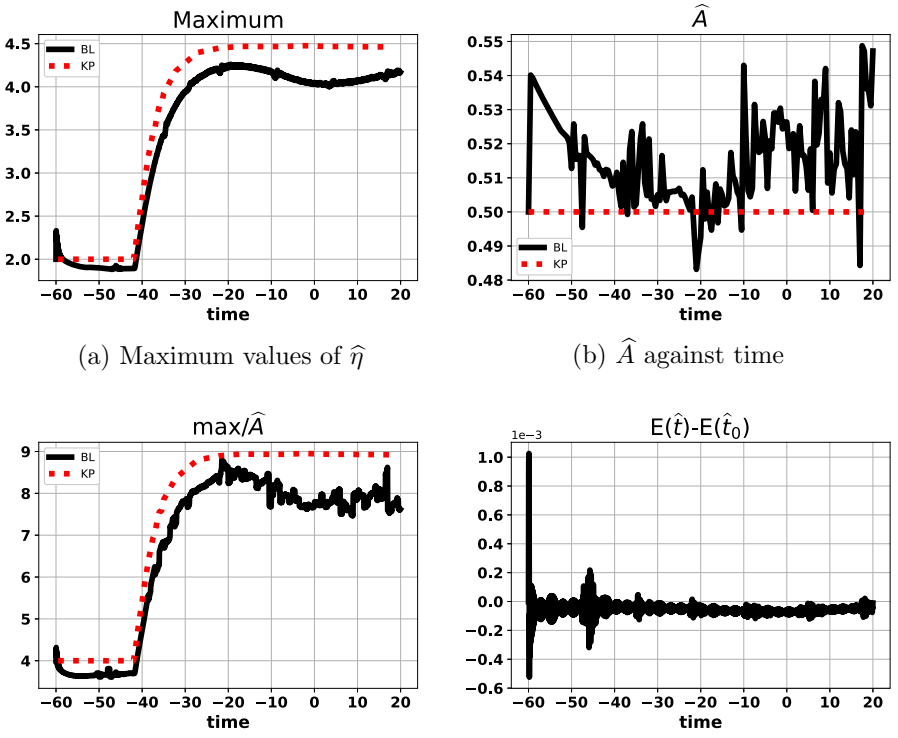

(a) Maximum values of $\widehat{\eta}$ (b) $\widehat{A}$ against time

(c) max/$\widehat{A}$ against time (d) Deviation of energy

Fig. 9 Results obtained for three-soliton simulations of the Benney–Luke equations (BLE-SP3) with $\epsilon = 0.05$, employing finite-element polynomials of order CG4. The red dashed line is computed from the rescaled KPE solution as a reference. Panels show: **a** maximum values of $\widehat{\eta}$ over time; **b** $\widehat{A} := \max_{\widehat{x}}(\widehat{\eta}(\cdot, \widehat{y} = 24, \widehat{t}))$; **c** amplification $\max(\widehat{\eta})/\widehat{A}$ against time; and **d** energy deviation $E(\widehat{t}) - E(\widehat{t}_0)$ in time for simulation BLE-SP3, where $E(\widehat{t})$ is defined in (6) for the BLE system and $\widehat{t}_0 = -60$. The energy deviation from $E(\widehat{t}_0) = 24.251$ is of the order of 10^{-4} except around $\widehat{t}_0$, which implies that the numerical scheme is stable

creates the time-dependent three-soliton with its maximum ninefold peak in space and time.

The 'standard' or base resolution used in the PFE simulations is determined as follows. We first choose the domain length and base mesh size in the y-direction as $L_y = (H_0/\sqrt{\mu})L_{y\mathrm{BLE}} = 40{,}000$ m and $\Delta y = \Delta y_{\mathrm{BLE}}(H_0/\sqrt{\mu}) = 200$ m, with $L_{y\mathrm{BLE}} = 20$ and $\Delta y_{\mathrm{BLE}} = 0.1$ (the remaining parameter values are given in the table of Fig. 13 caption). This results in a base number of elements in the y-direction equal to $N_y = L_y/\Delta y = 200$. The base mesh size in the x-direction, Δx, is chosen to be similar to Δy by selecting a number of elements as the nearest integer, N_x, to $L_x/\Delta y$, where $L_x = (H_0/\sqrt{\mu})L_{xBLE} = 17{,}725.6$ m and $L_{xBLE} = 8.863$. Therefore, the base mesh uses a number of degrees-of-freedom (DoFs) equal to $(n_h N_x)(n_h N_y + 1)(n_v N_z + 1) = (2\times 89)(2\times 200+1)(2\times 4+1) = 642,402$, where n_h, n_v is the order of base functions in the horizontal and vertical, respectively (in all simulations, we used $n_h = 2$ or 4 and $n_v = 2$; see also the discussion in the paragraph after Eq. (43). In addition, the base time step is $\Delta t = \Delta t_{\mathrm{BLE}}(H_0/\sqrt{gH_0\mu}) = 0.7139$ s, with $\Delta t_{\mathrm{BLE}} = 0.005$. Subsequently,

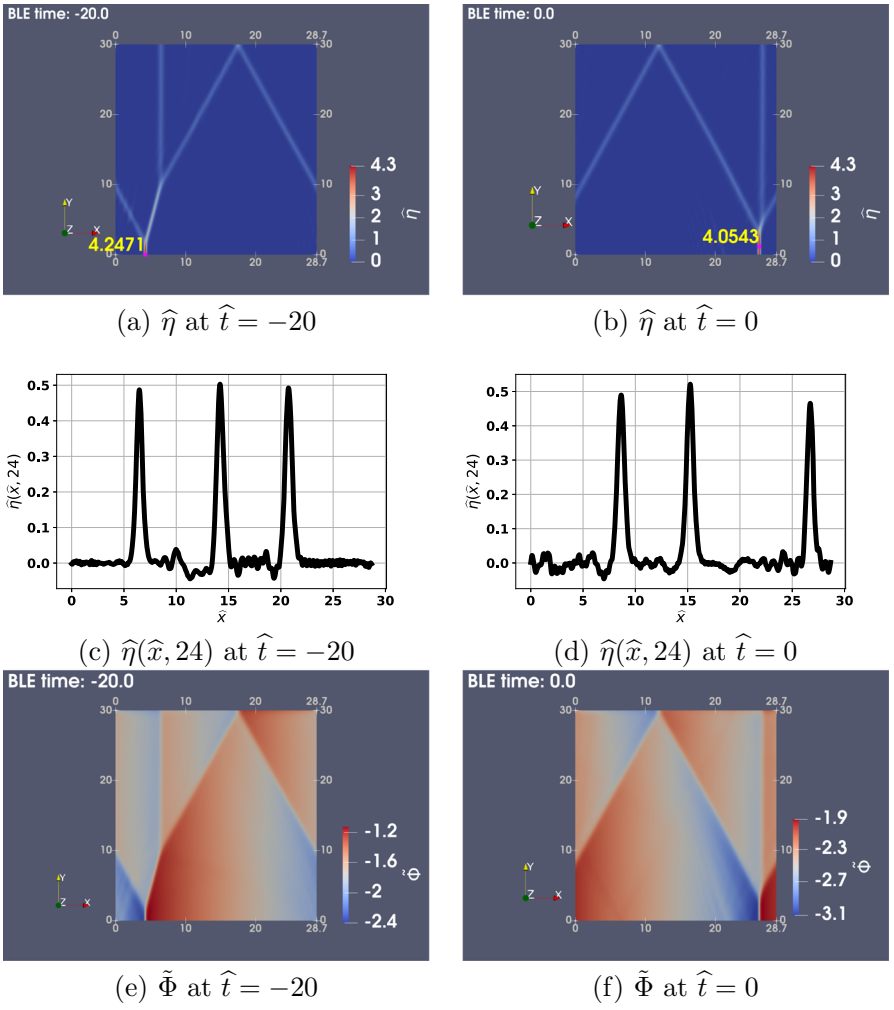

(a) $\widehat{\eta}$ at $\widehat{t} = -20$ (b) $\widehat{\eta}$ at $\widehat{t} = 0$

(c) $\widehat{\eta}(\widehat{x}, 24)$ at $\widehat{t} = -20$ (d) $\widehat{\eta}(\widehat{x}, 24)$ at $\widehat{t} = 0$

(e) $\tilde{\Phi}$ at $\widehat{t} = -20$ (f) $\tilde{\Phi}$ at $\widehat{t} = 0$

Fig. 10 Numerical three-soliton solution for the Benney–Luke equations (BLE-SP3) for $\epsilon = 0.05$ at times $\widehat{t} = -20$ (left-hand side panels) and $\widehat{t} = 0$ (right-hand side panels), respectively. Panels **a** and **b** show the surface elevation $\widehat{\eta}$ which is seen to attain a global maximum at $\widehat{t} = -20$. Panels **c** and **d** show that the height of $\widehat{\eta}$ in the far-field $\widehat{y} = 24$ is close to the initial height 0.5 at both times. Panels **e** and **f** show the potential $\tilde{\Phi}$

we refine resolution to check convergence of the simulation undertaken with the lowest resolution presented, i.e., denoted by "CG2/$\frac{\Delta y}{3}$". For spatial refinement, we take $N_y = pL_y/\Delta y$ (with $p > 1$) elements in the y-direction and appropriately choose a number of elements in the x-direction, N_x to retain the scaling $\Delta x \approx \Delta y$. The DoFs for all the refined simulations are given in the table of Fig. 13 caption.

Two groups of numerical results are shown in Fig. 11; snapshots (a)–(d) display the fields of surface elevation η and free-surface velocity potential $\tilde{\psi}$ at the mid- and

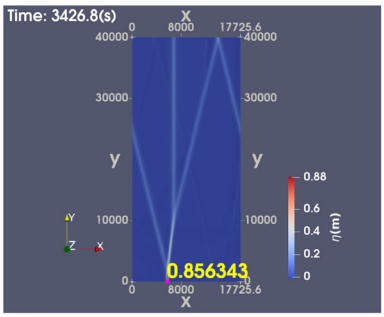

(a) η at $t = 3426.8$s with CG2 and $\frac{\Delta y}{3}$

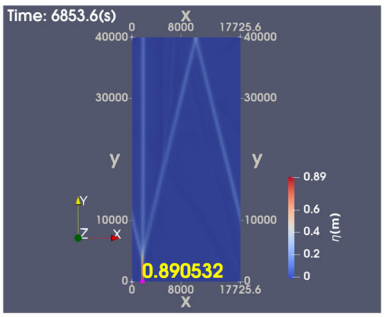

(b) η at $t = 6853.6$s with CG2 and $\frac{\Delta y}{3}$

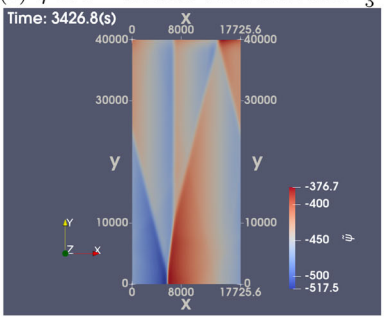

(c) $\tilde{\psi}$ at at $t = 3426.8$s with CG2 and $\frac{\Delta y}{3}$

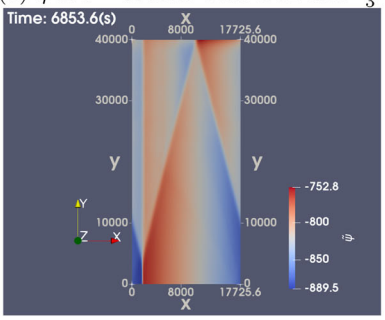

(d) $\tilde{\psi}$ at $t = 6853.6$s with CG2 and $\frac{\Delta y}{3}$

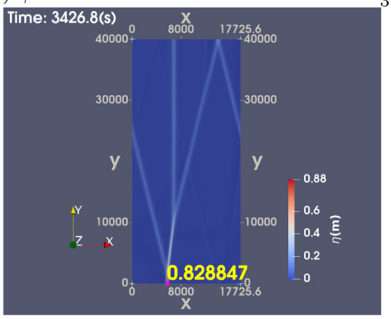

(e) η at $t = 3426.8$s with CG4 and $\frac{2\Delta y}{3}$

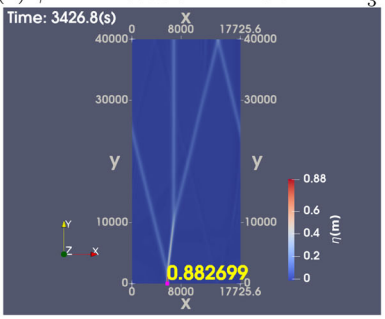

(f) η at $t = 3426.8$s with CG2, $\frac{\Delta y}{3}$ and $\frac{\Delta t}{2}$

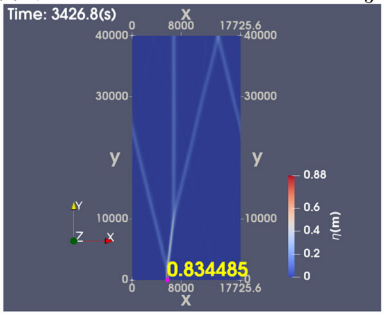

(g) η at $t = 3426.8$s with CG2 and $\frac{\Delta y}{4}$

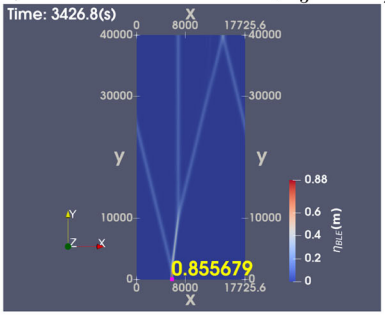

(h) Re-scaled η_{BLE} at $t = 3426.8$s

Fig. 11 Numerical results of η and $\tilde{\psi}$ obtained from a potential-flow simulation of three-soliton interactions (PFE-SP3) with $\epsilon = 0.01$. **a**–**d** used CG2 basis functions with spatial step $\Delta x \approx \Delta y = 200$ m and time step $\Delta t = 0.7139$ s, and **e**–**h** are η at $t = 3426.8$ s using different basis functions and spatial-temporal resolution as indicated in panel sub-captions

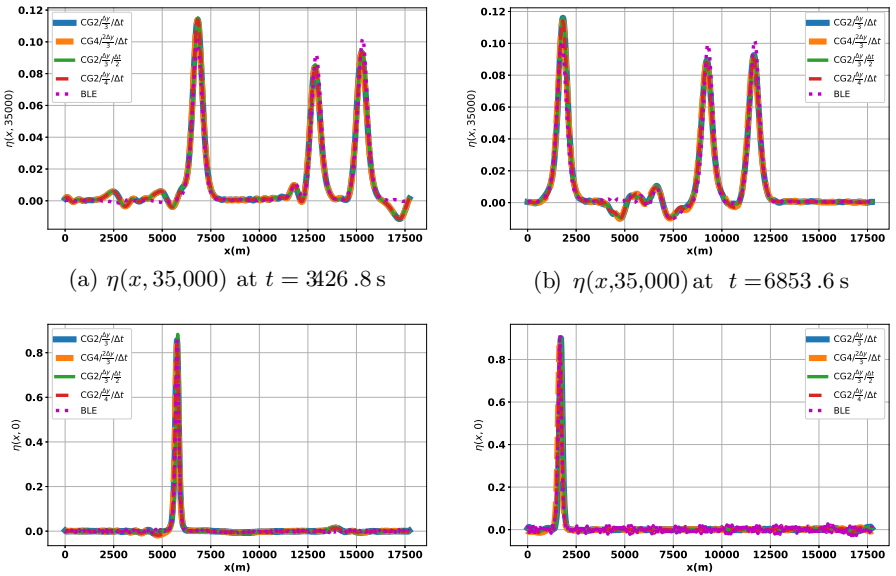

(a) $\eta(x, 35{,}000)$ at $t = 3426.8$ s (b) $\eta(x, 35{,}000)$ at $t = 6853.6$ s

(c) $\eta(x, 0)$ at $t = 3426.8$ s (d) $\eta(x, 0)$ at $t = 6853.6$ s

Fig. 12 Cross-sections of η from PFE-SP3 with $\epsilon = 0.01$. All curves are close to each other which implies that the resolution seems to be converged. Panels **a** and **b** show that the height of η in the far-field $y = 35{,}000$ m is close to the initial height 0.1 m at both times $t = 3426.8$ s and $t = 6853.6$ s. Panels **c** and **d** depict that the height of η at the bottom boundary $y = 0$ m, at time $t = 3426.8$ s and $t = 6853.6$ s, respectively. In each case, the free surface attains a height of about 0.82 m and 0.89 m, respectively

end-run times of a simulation using CG2 basis functions; and (e)–(h) demonstrate the surface elevation η for various spatial and time resolutions. In addition, cross-sections of η at $y = 35{,}000$ m and $y = 0$ m are depicted in Fig. 12. It can be observed from the similarity of the various curves displaying η that spatial convergence is achieved. Further results of the simulations and the exact KPE solution are displayed in the panels of Fig. 13 for various spatial resolutions, time steps, and basis functions: the maximum of η over time, the far-field estimate of amplitude A at $y = 35{,}000$ m over time, the maximum amplification over time as the ratio thereof as well as the relative-energy deviation. The amplification oscillates between about 7.6 to 8.25 due to dispersive effects, possibly due to the weaker dispersion and stronger nonlinearity in the PFE. The relative-energy deviations are small and appear to decrease for the higher resolutions, which is indicative of a stable simulation. It should be noted that smaller spatial resolutions in y-directions are required to get convergent results; here, $\Delta y/3$ is deemed to be sufficient.

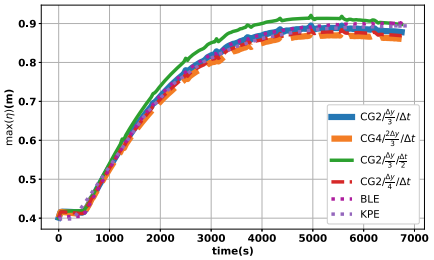

(a) Maximum with $\epsilon = 0.01$, $\tilde{A} = 0.5\left(\frac{3}{4}\right)^{1/3}$

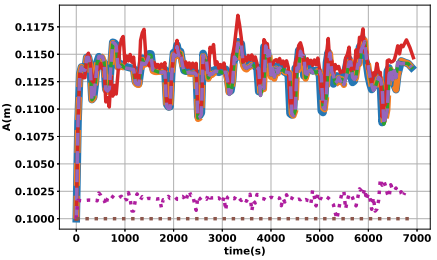

(b) A against time

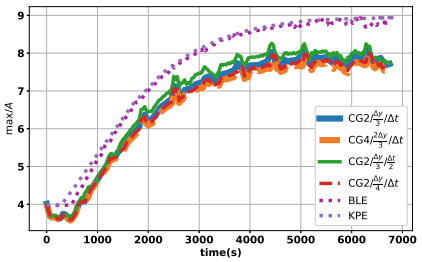

(c) $\max/A$ over time

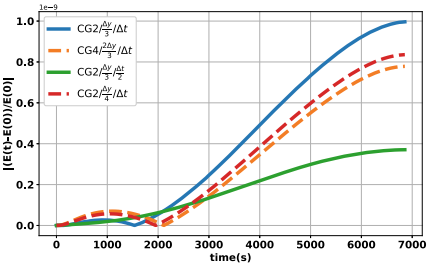

(d) Relative energy error

Simulation	⊠	δ	L_x (m)	L_y (m)	$L_z = H_0$ (m)	T (s)	Δt_{BLE}	N_x	N_y	N_z	DoFs	Run time (min)
PFE CG2/ $\frac{\Delta y}{3}/\Delta t$	0.01	10^{-5}	17725.6	40,000	20	6855	0.005	266	600	4	5,750,388	2880
PFE CG4/ $\frac{2\Delta y}{3}/\Delta t$	0.01	10^{-5}	17725.6	40,000	20	6855	0.005	133	300	4	5,750,388	5588
PFE CG2/ $\frac{\Delta y}{4}/\Delta t$	0.01	10^{-5}	17725.6	40,000	20	6855	0.005	355	800	4	10,230,390	5383
PFE CG2/ $\frac{\Delta y}{3}/\frac{\Delta t}{2}$	0.01	10^{-5}	17725.6	40,000	20	6855	0.0025	266	600	4	5,750,388	6094.6
BLE: CG2/ $\frac{\Delta y}{3}/\Delta t$	0.01	10^{-5}	17725.6	40,000	20	6855	0.005	266	600	-	-	396

Fig. 13 Results obtained from a potential-flow simulation of three-soliton interactions (PFE-SP3) with varying spatial resolution. The simulation employs parameters in the table above. We set the base resolutions in space and time as $\Delta x \approx \Delta y = 200$ m, $\Delta t = \Delta t_{\text{BLE}}(H_0/\sqrt{gH_0\epsilon^2}) \approx 0.005 \times 142.78 = 0.7139$ s where $g = 9.81\ \text{m/s}^2$. In addition, the initial far-field amplitude of each soliton was set to $\tilde{A} = 0.5\left(\frac{3}{4}\right)^{1/3}$, so that $A = 0.1$ m (cf. (2) and (11a). Key to colours: blue—CG2 basis functions with $\frac{\Delta y}{3}$ and Δt; orange—CG4 with $\frac{2\Delta y}{3}$ and Δt; green—CG2 with $\frac{\Delta y}{3}$ and $\frac{\Delta t}{2}$; red—CG2 with $\frac{\Delta y}{4}$ and Δt (relative to base resolution). Note that the basis functions quoted above refer to the horizontal direction only; in the vertical direction, CG2 is always used. The purple and brown curves, respectively, denote rescaled BLE and KPE solutions, used as reference. Panels show: **a** maximum values of η over time; **b** $A := \max_x(\eta(\cdot, y = 35{,}000\ \text{m}, t))$; **c** amplification $\max(\eta)/A$ against time; and **d** relative-energy error $|1 - E(t)/E(0)|$. All the initial total energies $E(0)$ are the same, -2.782×10^{13} up to five digits. Run times given are for simulations using 40 cores on arc4 HPC. We note that the simulation on the second row requires a much longer run time than the first simulation, despite having the same DoFs, and this is caused by the CG4 basis functions that lead to denser operator matrices

5.3 Comparison of Simulations

Figure 13 also presents a comparison between simulations of the BLE and the PFE, both using $\epsilon = 0.01$, $\delta = 10^{-5}$, $ac = 1$ (we note that in Fig. 8 for BLE, a smaller value $\delta = 10^{-10}$ was used). The comparison reveals different amplifications at (8.8, 9) and (7.6, 8.25) for BLE and PFE, respectively. The more intensified oscillations seen in the latter are thought to be due to the stronger nonlinearity and weaker dispersion

in the PFE, relative to those in the BLE and the KPE. At present, PFE simulations for larger $\epsilon = 0.05$ and $\widehat{A} = 0.5$—as performed for the BLE and shown in Fig. 9—are not attainable without wave-breaking parameterisations and/or a more advanced treatment of the numerical or exact KPE solution for periodic channel domains.

6 Concluding Remarks

In the present investigation, we generated extreme waves arising from interaction of three line-solitons with equal far-field amplitudes by seeding, with exact solutions of the Kadomtsev–Petviashvili equation (KPE), finite-element solvers based on two water-wave models, i.e., the Benney–Luke equations (BLE) and the more advanced potential-flow water-wave equations (PFE). We have additionally developed new analytical results on the theoretical ninefold maximum amplification of the KPE, and have moreover established that an amplification factor of circa (7.6, 9) for three interacting solitons can be reached in numerical simulations of the BLE and PFE.

We have carried out two sets of simulations using soliton wave amplitudes computed with $\epsilon = 0.01, 0.05$. To set up these simulations, we seeded them with an exact solution of the Kadomtsev–Petviashvili equation (KPE) at the time when the amplification is fourfold relative to the far-field soliton amplitude. An advanced analysis has been presented to prove that this KPE solution consists of three-soliton interactions that can reach a ninefold amplification at a later point in space and time, which discovery both removes a spatial divergence from our previous analysis [13] and also enables results to be computed with higher amplifications in our newest simulations. The simulations with $\epsilon = 0.05$ are reasonably realistic inasmuch as the far-field soliton amplitude is then 0.5 m when the rest depth is taken as $H_0 = 20$ m under the scaling (2); these parameters yield a simulated peak wave of about 3.5 to 4 m, while the peak in the KPE would reach 4.5^{-} m.

To conduct the PFE simulations, we have employed a pseudo-computer-algebraic approach of directly implementing the relevant time-discrete variational principles (VP) within the finite-element framework *Firedrake*. That led to a spatially spectrally accurate water-wave model with second-order accuracy in time. The direct implementation of the time-discrete VPs reduced time-to-development while closely following the mathematics; additionally, the respective weak formulations of the discrete equations were generated automatically by Firedrake, thereby avoiding derivation of cumbersome expressions of the weak forms and hence circumventing the potential introduction of human error. Subsequent optimisation of the solver pre-conditioners for the nonlinear equations gave a speed-up factor in the interval [4, 9] on both laptops and HPC computers.

The simulation with the PFE revealed an amplification of ~ 7.8—relative to those in the BLE of (8.8, 9)—for amplitude of $A = 0.1$ m (both for $\epsilon = 0.01$). Higher amplitudes are presently not (yet) achievable in the current channel-periodic domain and set-up, and/or without wave-breaking parameterisations. Despite our computational advances, it was difficult to achieve simulations of higher amplitude waves with acceptable stability, as evidenced by monitoring the temporal evolution of energy fluctuations that should be devoid of a systematic drift. The number of required degrees-of-freedom

for the PFE simulations is large, and the narrow- and high-peak amplitudes demanded a level of resolution that has hampered matters. The difficulty of finding adequate resolutions may have been caused by the manner in which we incorporated the x-periodicity, since the background velocity-potential fields $U_0(y, z)x$ used to achieve that periodicity for the variables representing the velocity-potential deviations created numerical sensitivity at the top corners of the channel.

One potential way to deal with the stronger nonlinearity experienced in the PFE is to include all higher order terms in (12) and (13), such that the initialisation is improved, given that we noticed a strong difference in dispersion between the KPE-BLE models and the PFE at higher values of ϵ and $\mu(=\epsilon^2)$. Another way to avert this sensitivity at the top corners is to analyse exact or semi-analytical cnoidal-wave versions of the KPE solution on an infinite plane, and to use these to seed BLE and PFE simulations. However, these exact solutions could be more complicated [29] than the approach presently adopted and so it remains to be seen whether a proof of exact fourfold and ninefold amplifications can be derived for such two and three cnoidal-wave interactions.[4]

Finally, further extensions of the present work will be directed towards establishing not only simulations and a design to support experimental validation, but also faster computational solvers through improved pre-conditioning and non-uniform mesh refinement.

Acknowledgements It is a pleasure to thank Colin Cotter and Koki Sagiyama of the Firedrake team for their valuable assistance as well as the numerous other people who kindly answered our queries on the Firedrake Slack channel. Colin Cotter in particular designed the pre-conditioner used; see Appendix C.3.1.

Author Contributions The idea to examine maximum amplification of three-soliton interactions analytically and numerically arose after discussions between OB and Prof Yuji Kodama at a workshop in Dresden, Germany, 2011. OB developed the numerics/mathematics of (time-discrete) VPs for both BLE and PFE, including the new MMP and SV time discretisations, OB implemented matters in a new 3D Firedrake code, and wrote the first draft of the paper excluding the section on computer algebra; JC assisted in finalising the new 3D Firedrake code, set up, and performed the HPC calculations at the University of Leeds, provided the higher order $\mathcal{O}(\epsilon, \mu^4)$ BLE corrections and aspects of the SP2/SP3 initialisation; MK worked out (and wrote the section on) the computer algebra of the maximum amplification in discussion with OB who provided the geometric proof and additional (not shown in the main text) numerical Python verification; MK meticulously edited the entire paper; AK wrote the initial KPE-SP3 solution and formulated the new SP3 cases, thoroughly edited, checked, streamlined and finalised the paper, and provided assistance in the BLE simulations using AK's original code; YL worked on parallel formulations and simulations using the PFE weak-formulation approach of [22] and double-checked a few MMP-HPC-PFE-simulations; YL also meticulously checked the formulas and numerical codes.

Funding YL, MK, and OB acknowledge support via an EU project "*Eagre: high-seas wave-impact modelling*" (GA859983) and JC via a Sejong Science Fellowship Grant "*Research on approximate hierarchy among abnormal wave models*" (2021R1C1C2008763), funded by the National Research Foundation of Korea and the Korean government (MSIT). JC used the arc4-HPC from the University of Leeds during a partially funded visit in 2023.

Data Availability The codes used to produce the results of this paper can be found at https://github.com/cjunho/cjh/tree/master, and https://zenodo.org/records/10459706. Additional code development is available at https://github.com/obokhove/EagreEUEID20202023/tree/master/potflowVP.

[4] See also the KP-page: https://web.archive.org/web/20060206111407/http://www.amath.washington.edu/~bernard/kp.html.

Declarations

Conflict of Interest The authors declare that they have no conflict of interest.

Appendix A: Higher Order Terms in BLE/KPE-Initialisation

Initialisation of the Benney–Luke equations (BLE) and potential-flow equations (PFE) can be improved by including higher order terms in ϵ. We therefore provide (known) yet lengthy details on the expansions to define this improved initialisation.

Substituting (7a), (7b) into (5a) yields

$$\begin{aligned}
\widehat{\eta}(\widehat{x},\widehat{y},\widehat{t}) &= -\partial_{\widehat{t}}\Phi - \frac{\epsilon^2}{2}\partial_{\widehat{x}}^3\Phi - \frac{\epsilon}{2}\left(\partial_{\widehat{x}}\Phi\right)^2 \\
&\quad + \left\{\frac{\epsilon^2}{2}\left(\partial_{\widehat{x}}^2\partial_{\widehat{t}}\Phi + \partial_{\widehat{y}}^2\partial_{\widehat{t}}\Phi - \partial_{\widehat{x}}\partial_{\widehat{y}}^2\Phi\right) - \frac{\epsilon}{2}\left(\partial_{\widehat{y}}\Phi\right)^2\right\} \\
&= \left(\frac{2^4}{3^2}\right)^{1/6}\partial_X\Psi \\
&\quad + \epsilon\left(-\left(\frac{2^8}{3^4}\right)^{1/6}\partial_\tau\Psi - \left(\frac{3^2}{2^4}\right)^{1/6}\partial_X^3\Psi - \left(\frac{2^2}{3^4}\right)^{1/6}\left(\partial_X\Psi\right)^2\right) \\
&\quad + \epsilon^2\left(\partial_X^2\partial_\tau\Psi - \frac{3}{2}\partial_X\partial_Y^2\Psi - \left(\partial_Y\Psi\right)^2\right) + \epsilon^3\left(\frac{3^4}{2^2}\right)^{1/6}\partial_Y^2\partial_\tau\Psi \\
&= \left(\frac{2^4}{3^2}\right)^{1/6}u + \epsilon u_1 + \mathcal{O}(\epsilon^2),
\end{aligned} \tag{A1}$$

wherein we defined

$$u_1 = -\left(\frac{2^8}{3^4}\right)^{1/6}\partial_\tau\Psi - \left(\frac{3^2}{2^4}\right)^{1/6}\partial_X^3\Psi - \left(\frac{2^2}{3^4}\right)^{1/6}\left(\partial_X\Psi\right)^2. \tag{A2}$$

Similarly, we substitute (7a) into (5b) to find

$$0 = \partial_{\widehat{t}}\widehat{\eta} - \frac{\epsilon^2}{2}\partial_{\widehat{t}}\nabla^2\widehat{\eta} + \nabla\cdot\left(\left(1+\epsilon\widehat{\eta}\right)\nabla\Phi\right) - \frac{2}{3}\epsilon^2\Delta^2\Phi \tag{A3}$$

$$
\begin{aligned}
&= \sqrt{\frac{1}{\epsilon}}\Bigg[-\left(\frac{3^2}{2}\right)^{1/6}\partial_X\widehat{\eta} + \sqrt{2}\epsilon\,\partial_\tau\widehat{\eta} + \epsilon\left(\frac{3^6}{2^9}\right)^{1/6}\partial_X^3\widehat{\eta} \\
&\quad + \sqrt{\frac{1}{\epsilon}}\Bigg(\left(\frac{3^4}{2^2}\right)^{1/6}\partial_X^2\Phi + \epsilon\left(\frac{3^8}{2^4}\right)^{1/6}\partial_Y^2\Phi + \epsilon\left(\frac{3^4}{2^2}\right)^{1/6}\partial_X\widehat{\eta}\,\partial_X\Phi \\
&\quad + \epsilon\left(\frac{3^4}{2^2}\right)^{1/6}\widehat{\eta}\,\partial_X^2\Phi - \epsilon\,6^{1/3}\partial_X^4\Phi\Bigg) + \mathcal{O}(\epsilon^2)\Bigg]. \qquad \text{(A4)}
\end{aligned}
$$

Using (7b) and (A1), the above becomes

$$
\begin{aligned}
0 &= \sqrt{\frac{1}{\epsilon}}\Bigg[-\left(\frac{3^2}{2}\right)^{1/6}\partial_X\Big(\left(\frac{2^4}{3^2}\right)^{1/6}u + \epsilon u_1\Big) + \epsilon\left(\frac{2^7}{3^2}\right)^{1/6}\partial_\tau u + \epsilon\left(\frac{3^4}{2^5}\right)^{1/6}\partial_X^3 u \\
&\quad + \left\{2^{3/6}\partial_X^2\Psi + \epsilon(2\cdot 3^4)^{1/6}\partial_Y^2\Psi + \epsilon\left(\frac{2^7}{3^2}\right)^{1/6}\partial_X u\,\partial_X\Psi + \epsilon\left(\frac{2^7}{3^2}\right)^{1/6}u\,\partial_X^2\Psi\right\} \\
&\quad - \left(\frac{2^7}{3^2}\right)^{1/6}\epsilon\partial_X^4\Psi + \mathcal{O}(\epsilon^2)\Bigg] \\
&= \sqrt{\frac{1}{\epsilon}}\Bigg[-\left(\frac{3^2}{2}\right)^{1/6}\partial_X\Big(\left(\frac{2^4}{3^2}\right)^{1/6}u + \epsilon u_1\Big) + 2^{3/6}\partial_X^2\Psi \\
&\quad + \epsilon\left\{\left(\frac{2^7}{3^2}\right)^{1/6}\partial_\tau u + \left(\frac{3^4}{2^5}\right)^{1/6}\partial_X^3 u + (2\cdot 3^4)^{1/6}\partial_Y^2\Psi\right. \\
&\quad \left. + \left(\frac{2^7}{3^2}\right)^{1/6}\partial_X u\,\partial_X\Psi + \left(\frac{2^7}{3^2}\right)^{1/6}u\,\partial_X^2\Psi - \left(\frac{2^7}{3^2}\right)^{1/6}\partial_X^4\Psi\right\} + \mathcal{O}(\epsilon^2)\Bigg]. \qquad \text{(A5)}
\end{aligned}
$$

Substitution of (7c) and u_1 into the above leads to the interim result

$$
\begin{aligned}
0 &= \sqrt{\frac{1}{\epsilon}}\Bigg[-\left(\frac{3^2}{2}\right)^{1/6}\partial_X\left\{\left(\frac{2^4}{3^2}\right)^{1/6}\partial_X\Psi\right\} \\
&\quad -\epsilon\left(\frac{3^2}{2}\right)^{1/6}\partial_X\left\{-\left(\frac{2^8}{3^4}\right)^{1/6}\partial_\tau\Psi - \left(\frac{3^2}{2^4}\right)^{1/6}\partial_X^3\Psi - \left(\frac{2^2}{3^4}\right)^{1/6}(\partial_X\Psi)^2\right\} \\
&\quad +2^{3/6}\partial_X^2\Psi + \epsilon\left\{\left(\frac{2^7}{3^2}\right)^{1/6}\partial_\tau\partial_X\Psi + \left(\frac{3^4}{2^5}\right)^{1/6}\partial_X^4\Psi + (2\times 3^4)^{1/6}\partial_Y^2\Psi\right. \\
&\quad \left. +2\left(\frac{2^7}{3^2}\right)^{1/6}\partial_X\Psi\,\partial_X^2\Psi - \left(\frac{2^7}{3^2}\right)^{1/6}\partial_X^4\Psi\right\} + \mathcal{O}(\epsilon^2)\Bigg] \\
&= \sqrt{\frac{1}{\epsilon}}\Bigg[\epsilon\left\{\left(\frac{2^7}{3^2}\right)^{1/6}\partial_X\partial_\tau\Psi + \left(\frac{3^4}{2^5}\right)^{1/6}\partial_X^4\Psi + \left(\frac{2}{3^2}\right)^{1/6}\partial_X(\partial_X\Psi)^2\right\}
\end{aligned}
$$

$$+\epsilon\left\{\left(\frac{2^7}{3^2}\right)^{1/6}\partial_\tau\partial_X\Psi+\left(\frac{3^4}{2^5}\right)^{1/6}\partial_X^4\Psi+(2\times 3^4)^{1/6}\partial_Y^2\Psi\right.$$
$$\left.+\left(\frac{2^7}{3^2}\right)^{1/6}\partial_X\left(\partial_X\Psi\right)^2-\left(\frac{2^7}{3^2}\right)^{1/6}\partial_X^4\Psi\right\}+\mathcal{O}(\epsilon^2)\Bigg]. \tag{A6}$$

Finally, by rearranging the above, it transpires that

$$\begin{aligned}0&=\sqrt{\frac{1}{\epsilon}}\left(\frac{2}{3^2}\right)^{1/6}\left[\epsilon\left\{2\partial_X\partial_\tau\Psi+\frac{3}{2}\partial_X^4\Psi+\partial_X\left(\partial_X\Psi\right)^2\right\}\right.\\&\quad\left.+\epsilon\left\{2\partial_\tau\partial_X\Psi+\frac{3}{2}\partial_X^4\Psi+3\partial_Y^2\Psi+2\partial_X\left(\partial_X\Psi\right)^2-2\partial_X^4\Psi\right\}+\mathcal{O}(\epsilon^2)\right]\\&=\sqrt{\frac{1}{\epsilon}}\left(\frac{2}{3^2}\right)^{1/6}\left[\epsilon\left\{\partial_X\left(4\partial_\tau\Psi+3\left(\partial_X\Psi\right)^2+\partial_X^3\Psi\right)+3\partial_{YY}\Psi\right\}+\mathcal{O}(\epsilon^2)\right].\end{aligned} \tag{A7}$$

Using $u=\partial_X\Psi$, cf. (7c), the terms of leading-order $\mathcal{O}(\epsilon)$ in the last line of (A7) together yield the well-known KPE [7] in the "standard" form (8) stated in the main text.

Appendix B: Details of Soliton Dynamics

Detailed information on the numerical verification of soliton dynamics in the Benney–Luke equations (BLE) and potential-flow equations (PFE) is provided for the following cases in an x-periodic domain:

- SP1: a single soliton;
- SP2: two-soliton interaction with a maximal fourfold amplification; and,
- SP3: three-soliton interactions with a maximal ninefold amplification.

In each case, the BLE and PFE are seeded with an exact solution of the KPE—at a suitable initial time that is well prior to the maximum amplification in the SP3 case—using the asymptotic expressions for the velocity potential up to $\mathcal{O}(\mu)$ or $\mathcal{O}(\mu^2)$ in the BLE expansion.

B.1 SP1: Single Soliton

The soliton used in the BLE ((68) in [12]) reads

$$\tilde{q}(\tilde{x},\tilde{t})=\frac{1}{2}\sqrt{(c\epsilon/\mu)}\left(\tilde{x}-\tilde{x}_0-(1+\epsilon c/6)\tilde{t}\right) \tag{B8a}$$
$$\tilde{\eta}(\tilde{x},\tilde{t})=\frac{1}{3}c\,\mathrm{sech}^2 q \tag{B8b}$$
$$\tilde{\Phi}(\tilde{x},\tilde{t})=\frac{2}{3}\sqrt{(c\mu/\epsilon)}(1+\tanh q) \tag{B8c}$$

with the transformed coordinates variables used in the BLE framework denoted via tildes. To recap, the scaling and its inverse are (see Sect. 2)

$$\phi = \frac{\epsilon H_0\sqrt{gH_0}}{\sqrt{\mu}}\tilde{\phi}, \quad \eta = \epsilon H_0\tilde{\eta}, \quad z = H_0\tilde{z}, \quad x = \frac{H_0}{\sqrt{\mu}}\tilde{x}, \quad t = \frac{H_0}{\sqrt{gH_0\mu}}\tilde{t}, \tag{B9a}$$

$$\tilde{\phi} = \frac{\sqrt{\mu}}{\epsilon H_0\sqrt{gH_0}}\phi, \quad \tilde{\eta} = \frac{1}{\epsilon H_0}\eta, \quad \tilde{z} = \frac{1}{H_0}z, \quad \tilde{x} = \frac{\sqrt{\mu}}{H_0}x, \quad \tilde{t} = \frac{\sqrt{gH_0\mu}}{H_0}t. \tag{B9b}$$

Hence, using the expansion of the solution in the vertical for BLE, the dimensional asymptotic solutions for the PFE are as follows:

$$q(x,t) = \frac{1}{2}\sqrt{(c\epsilon/\mu)}\Big((\sqrt{\mu}/H_0)(x-x_0) - (1+\epsilon c/6)\frac{\sqrt{\mu g H_0}}{H_0}t\Big) \tag{B10a}$$

$$\eta(x,t) = \epsilon H_0\frac{1}{3}c\,\mathrm{sech}^2 q(x,t) \tag{B10b}$$

$$\begin{aligned}\phi(x,z,t) &= \frac{\epsilon H_0\sqrt{gH_0}}{\sqrt{\mu}}\Big(\tilde{\Phi}(\tilde{x},\tilde{t}) - \frac{1}{2}\mu\tilde{z}^2\frac{\partial^2}{\partial\tilde{x}^2}\tilde{\Phi}(\tilde{x},\tilde{t}) + \mathcal{O}(\mu^2\tilde{z}^4)\Big)\\ &= \frac{\epsilon H_0\sqrt{gH_0}}{\sqrt{\mu}}\frac{2}{3}\sqrt{\frac{c\mu}{\epsilon}}\Big(1+\tanh q + \frac{\epsilon\mu z^2}{4H_0^2}\frac{\sinh q}{\cosh q^3}\Big)\end{aligned} \tag{B10c}$$

$$\psi(x,t) = \frac{\epsilon\sqrt{gH_0^3}}{\sqrt{\mu}}\frac{2}{3}\sqrt{\frac{c\mu}{\epsilon}}\Big(1+\tanh q + \frac{\epsilon\mu(H_0+\eta(x,t))^2}{4H_0^2}\frac{\sinh q(x,t)}{\cosh q(x,t)^3}\Big), \tag{B10d}$$

through which $\eta(x,0)$, $\psi(x,0)$ will be used to initialise the PFE simulations, since the interior $\phi(x,z,0)$ is slaved to the free surface via $\phi(x, H_0+\eta(x,t), t) = \psi(x,t)$, the bottom boundary condition and the Laplace equation. Periodicity in a domain $x \in [0, L_x]$ is enforced as follows:

$$\phi(x,z,t) = U_0(z)x + \tilde{\phi}(x,z,t) = U_0(z)x + \tilde{\psi}(x,t)\hat{\phi}(z) + \varphi(x,z,t) \tag{B11}$$

$$U_0(z) = \frac{\phi(x_2,z,0) - \phi(x_1,z,0)}{x_2 - x_1} \tag{B12}$$

with $\hat{\phi}(z = H_0 + \eta(x,t)) = 1$ and $\varphi(x, z = H_0 + \eta(x,t), t) = 0$.

A further transformation is required in the fixed computational domain

$$x = \xi, \quad z = h(\xi,t)\frac{\zeta}{H_0} = (H_0 + \eta(\xi,t))\frac{\zeta}{H_0}, \tag{B13}$$

with $\xi \in [0, L_x]$, $\zeta \in [0, H_0]$. The expressions required then become

$$q(\xi,t) = \frac{1}{2}\sqrt{(c\epsilon/\mu)}\Big((\sqrt{\mu}/H_0)(\xi-\xi_0) - (1+\epsilon c/6)\frac{\sqrt{\mu g H_0}}{H_0}t\Big) \tag{B14a}$$

$$\eta(\xi,t) = \epsilon H_0 \frac{1}{3} c \,\mathrm{sech}^2 q(\xi,t) \tag{B14b}$$

$$\phi(\xi,\zeta,t) = \frac{\epsilon H_0\sqrt{gH_0}}{\sqrt{\mu}}\frac{2}{3}\sqrt{\frac{c\mu}{\epsilon}}\left(1+\tanh q + \frac{\epsilon\mu\zeta^2(1+\eta/H_0)^2)}{4H_0^2}\frac{\sinh q}{\cosh q^3}\right) \tag{B14c}$$

$$\approx \frac{\epsilon H_0\sqrt{gH_0}}{\sqrt{\mu}}\frac{2}{3}\sqrt{\frac{c\mu}{\epsilon}}\left(1+\tanh q + \frac{\epsilon\mu\zeta^2}{4H_0^2}\frac{\sinh q}{\cosh q^3}\right) \tag{B14d}$$

$$\psi(\xi,t) = \frac{\epsilon\sqrt{gH_0^3}}{\sqrt{\mu}}\frac{2}{3}\sqrt{\frac{c\mu}{\epsilon}}\left(1+\tanh q + \frac{\epsilon\mu(1+\eta/H_0)^2}{4}\frac{\sinh q(\xi,t)}{\cosh q(\xi,t)^3}\right) \tag{B14e}$$

$$\approx \frac{\epsilon\sqrt{gH_0^3}}{\sqrt{\mu}}\frac{2}{3}\sqrt{\frac{c\mu}{\epsilon}}\left(1+\tanh q + \frac{\epsilon\mu}{4}\frac{\sinh q(\xi,t)}{\cosh q(\xi,t)^3}\right). \tag{B14f}$$

In a periodic domain, the definition of ϕ needs to be modified, for which we use the approximate expressions above, as follows:

$$\phi(\xi,\zeta,t) = U_0\left(\zeta\frac{(H_0+\eta(\xi,t)}{H_0}\right)\xi + \tilde{\phi}(\xi,\zeta,t) \tag{B14g}$$

$$\approx U_0(\zeta)\xi + \tilde{\psi}(\xi,t)\hat{\phi}(\zeta) + \varphi(\xi,\zeta,t) \tag{B14h}$$

$$\tilde{\psi}(\xi,t) = \frac{\epsilon\sqrt{gH_0^3}}{\sqrt{\mu}}\frac{2}{3}\sqrt{\frac{c\mu}{\epsilon}}\left(1+\tanh q + \frac{\epsilon\mu(1+\eta/H_0)^2}{4}\frac{\sinh q(\xi,t)}{\cosh q(\xi,t)^3}\right) - U_0\left(H_0+\eta(\xi,t)\right)\xi \tag{B14i}$$

$$\approx \frac{\epsilon\sqrt{gH_0^3}}{\sqrt{\mu}}\frac{2}{3}\sqrt{\frac{c\mu}{\epsilon}}\left(1+\tanh q + \frac{\epsilon\mu}{4}\frac{\sinh q(\xi,t)}{\cosh q(\xi,t)^3}\right) - U_0(H_0)\xi, \tag{B14j}$$

with $\varphi(\xi, H_0, t) = 0, \hat{\phi}(H_0) = 1$ in the spatial coordinates (ξ,ζ) for the computational domain, such that $\tilde{\psi}$ is periodic in the ξ-direction. Note that for this test, there is in essence no z-dependence in U_0, since $\sinh q/\cosh^3 q$ decays sufficiently fast away from its centre in a sufficiently large domain. One could then decide to include the η-dependence in the initial $\tilde{\psi}$.

B.2 SP2: Two Interacting Solitons

The initial conditions (12) and (13) are transformations of a KPE solution of two-soliton interactions (SP2) with a fourfold amplification of the far-field incoming solitons. Employing Hirota's relation (9), it suffices to specify $K(X,Y,\tau)$. Following [6, 30] and in particular the same relation (14) and settings as in [13], we find that

$$K(X,Y,\tau) = (k_3-k_1)\,\mathrm{e}^{\theta_1}\left(\mathrm{e}^{\theta_3} + b\frac{(k_4-k_1)}{(k_3-k_1)}\mathrm{e}^{\theta_4}\right)$$

$$+ a(k_3 - k_2)\, \mathrm{e}^{\theta_2}\left(\mathrm{e}^{\theta_3} + b\frac{(k_4 - k_2)}{(k_3 - k_2)}\mathrm{e}^{\theta_4}\right), \tag{B15a}$$

$$=(\rightarrow_{a=b=1,k_3=k_2=0,k_4=-k_1=\tan\theta})\; k_4\left(\mathrm{e}^{\theta_1} + 2\mathrm{e}^{\theta_1+\theta_4} + \mathrm{e}^{\theta_4}\right) \tag{B15b}$$

$$= k_4\left(\mathrm{e}^{-k_4X+k_4^2Y+k_4^3\tau} + 2\mathrm{e}^{2k_4^2Y} + \mathrm{e}^{k_4X+k_4^2Y-k_4^3\tau}\right), \tag{B15c}$$

where $\theta_i = k_iX + k_i^2Y - k_i^3\tau$ with $i = 1, 2, 3, 4$, these k_i satisfying the relations $k_1 = -k_4 < k_2 = 0 = k_3 < k_4 = \tan\theta$ as well as $a = b = 1$; these choices yield the fourfold amplification. In particular, note that $\theta_1 + \theta_4$ does not depend on X. Here

$$k_4 = \tan\theta = \left(\frac{2}{9}\right)^{1/6}\frac{1}{4\sqrt{\epsilon}} \approx 8.7013 \times 10^{-1}$$

is the angle of the two top branches in the Y-shaped solution with the Y-axis, with $\epsilon = \mu^2 = 0.05$; see Fig. 14.

Additionally

$$K_X = k_4^2(\mathrm{e}^{\theta_4} - \mathrm{e}^{\theta_1}), \quad K_{XX} = k_4^3(\mathrm{e}^{\theta_4} + \mathrm{e}^{\theta_1}) \tag{B16a}$$

$$K_{XXX} = k_4^2K_X = k_4^4(\mathrm{e}^{\theta_4} - \mathrm{e}^{\theta_1}) \tag{B16b}$$

$$K_Y = k_4^3(\mathrm{e}^{\theta_4} + 4\mathrm{e}^{\theta_1+\theta_4} + \mathrm{e}^{\theta_1}) \tag{B16c}$$

$$K_{YY} = k_4^5(\mathrm{e}^{\theta_4} + 8\mathrm{e}^{\theta_1+\theta_4} + \mathrm{e}^{\theta_1}) \tag{B16d}$$

$$K_{XY} = k_4^4(\mathrm{e}^{\theta_4} - \mathrm{e}^{\theta_1}), \quad K_{XYY} = k_4^2K_{XY}. \tag{B16e}$$

For either BLE or PFE, using expressions (2) and (7), one then substitutes

$$X = \sqrt{\frac{\epsilon}{\mu}}\left(\frac{3}{\sqrt{2}}\right)^{1/3}(\widehat{x} - \widehat{t}) = \frac{\sqrt{\epsilon}}{H_0}\left(\frac{3}{\sqrt{2}}\right)^{1/3}\left(x - \sqrt{gH_0}t\right), \tag{B17a}$$

$$Y = \frac{\epsilon}{\sqrt{\mu}}\left(\frac{3}{\sqrt{2}}\right)^{2/3}\widehat{y} = \frac{\epsilon}{H_0}\left(\frac{3}{\sqrt{2}}\right)^{2/3}y, \tag{B17b}$$

$$\tau = \epsilon\sqrt{\frac{2\epsilon}{\mu}}\,\widehat{t} = \epsilon\sqrt{2\epsilon}\sqrt{g/H_0}t, \tag{B17c}$$

into the KPE-expressions to land in x, y, z, t-space.

In the respective far fields, these are three single-line-solitons with respective centrelines $X = -k_4Y + k_4^2\tau - \ln 2/k_4$, $X = k_4Y + k_4^2\tau + \ln 2/k_4$ and $X = k_4^2\tau$, found by the three pairs of combinations of the three terms involved in (B15b). Thus it follows that these lines intersect always at a fixed value of Y. Hence, we choose $\hat{y}_2 = -\hat{y}_1$ and, as in [13], we set $\hat{y}_2 = 20$. The periodic domain is determined by finding the $X_2 > X_1$ where $u(X_1, Y_2) = u(X_2, Y_2)$ and $u_X(X_1, Y_2) = u_X(X_2, Y_2) = 0$. To wit, by using relations (B16) one finds that

$$u_x = \frac{2}{K^3}\left(K^2K_{XXX} - 3KK_XK_{XX} + 2(K_X)^3\right) \tag{B18}$$

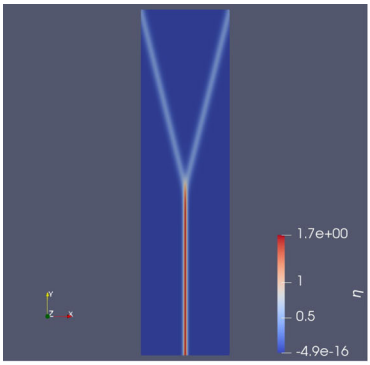

(a) η

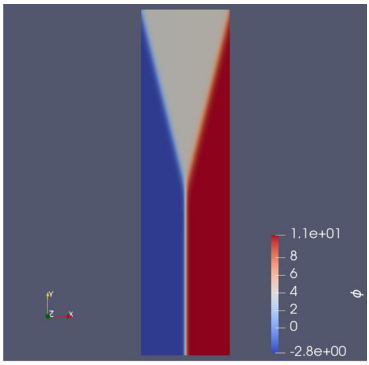

(b) ϕ at free surface

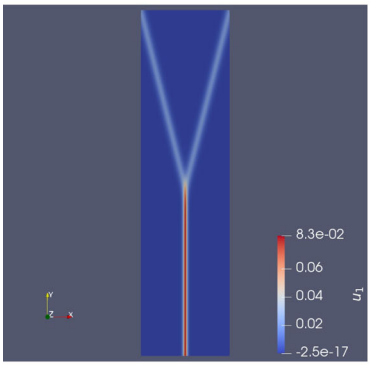

(c) u_1

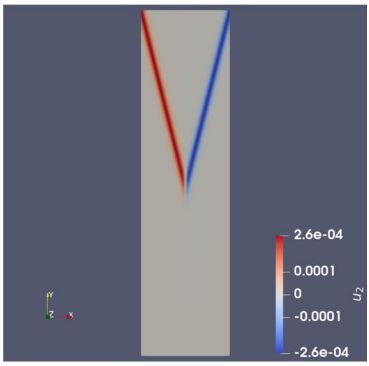

(d) u_2

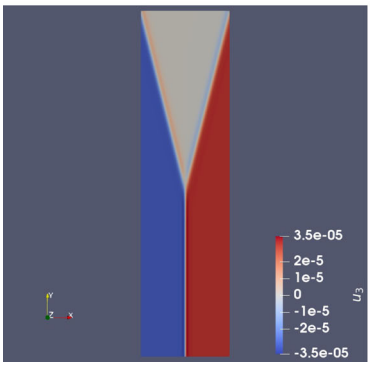

(e) u_3

Fig. 14 Top view of a sample initial condition and resulting velocity components for two-soliton interactions (SP2), calculated using (44) and (50) and shown at $\hat{t} = 0$ for $\epsilon = 0.05$, $\mu = \epsilon^2$, $H_0 = 20$ m

$$\propto 4 + \mathrm{e}^{\theta_1} + \mathrm{e}^{\theta_4} - 2\mathrm{e}^{\theta_1+\theta_4}, \tag{B19}$$

which expression set to zero at a given $Y = Y_2$ and time τ_0 yields

$$X_{1,2} = k_4^2\,\tau_0 \pm \frac{1}{k_4}\mathrm{acosh}\Big(\mathrm{e}^{k_4^2 Y_2} - 2\mathrm{e}^{-k_4^2 Y_2}\Big), \tag{B20}$$

since the acosh function yields two symmetric solutions and since $\theta_1 + \theta_4$ does not depend on X given that $k_1 = -k_4$. The scaling (2) then yields

$$y_2 = \frac{H_0}{\sqrt{\mu}}\widehat{y}_2, \tag{B21}$$

$$x_{1,2} = \frac{H_0}{\sqrt{\mu}}\widehat{x}_{1,2} = \frac{H_0}{\sqrt{\mu}}\left(\sqrt{\frac{\mu}{\epsilon}}\Big(\frac{\sqrt{2}}{3}\Big)^{\frac{1}{3}} X_{1,2} + \frac{1}{\epsilon}\sqrt{\frac{\mu}{2\epsilon}}\tau_0\right), \tag{B22}$$

where for this two-soliton interaction SP2, we choose $\widehat{y}_2 = 20$, $\tau_0 = 0$, $\epsilon = \mu^2 = 0.05$, $H_0 = 1$ m.

Since $\Phi = \sqrt{\epsilon}(4\sqrt{2}/9)^{1/3}\Psi$ (7) holds with $\Psi = 2\partial_x \ln K = 2K_X/K$ (10) and $\phi_0 = (\epsilon H_0\sqrt{gH_0}/\sqrt{\mu})\hat{\phi}_0$ (2) and using scalings (7) again, we find the potential-flow expressions (at the free surface)

$$\eta(x,y,t) = \epsilon H_0\hat{\eta} = 2\epsilon H_0\Big(\frac{4}{3}\Big)^{\frac{1}{3}} u = 2\epsilon H_0\Big(\frac{4}{3}\Big)^{\frac{1}{3}}\left(\frac{K_{XX}}{K} - \frac{K_X^2}{K^2}\right) \tag{B23a}$$

$$\psi(x,y,t) = \frac{\epsilon H_0\sqrt{gH_0}}{\sqrt{\mu}}\sqrt{\epsilon}\Big(\frac{4\sqrt{2}}{9}\Big)^{1/3}\left(\frac{2K_X}{K} - \frac{1}{2}\mu\frac{(H_0+\eta(x,y,t))^2}{H_0^2}\nabla^2_{\hat{x}\hat{y}}\left(\frac{2K_X}{K}\right)\right) \tag{B23b}$$

$$\phi(x,y,z,t) = \frac{\epsilon H_0\sqrt{gH_0}}{\sqrt{\mu}}\sqrt{\epsilon}\Big(\frac{4\sqrt{2}}{9}\Big)^{1/3}\left(\frac{2K_X}{K} - \frac{1}{2}\mu\frac{z^2}{H_0^2}\nabla^2_{\hat{x}\hat{y}}\left(\frac{2K_X}{K}\right)\right) \tag{B23c}$$

$$\nabla^2_{\hat{x}\hat{y}} = \left(\frac{\epsilon}{\mu}\left(\frac{3}{\sqrt{2}}\right)^{2/3}\partial_{XX} + \frac{\epsilon^2}{\mu}\left(\frac{3}{\sqrt{2}}\right)^{4/3}\partial_{YY}\right)\left(\frac{2K_X}{K}\right) \tag{B23d}$$

$$\partial_{XX}\left(\frac{2K_X}{K}\right) = 2\Big(\frac{K_{XXX}}{K} - 3\frac{K_{XX}K_X}{K^2} + 2\frac{K_X^3}{K^3}\Big) \tag{B23e}$$

$$\partial_{YY}\left(\frac{2K_x}{K}\right) = 2\Big(\frac{K_{XYY}}{K} - 2\frac{K_{XY}K_Y}{K^2} - \frac{K_XK_{YY}}{K^2} + 2\frac{K_XK_Y^2}{K^3}\Big) \tag{B23f}$$

$$U_0(y,z) = \frac{\phi(x_2,y,z,t_0) - \phi(x_1,y,z,t_0)}{x_2 - x_1} \tag{B23g}$$

$$\tilde{\psi}(x,y,t) = \psi(x,y,t) - U_0(y, H_0+\eta(x,y,t))x. \tag{B23h}$$

Table 2 KPE parameter values employed in the simulations undertaken

Simulation	ϵ	μ	$\tan\theta$	$\tilde{A}$	k_1	k_2	k_3
PFE-SP2	0.05	ϵ^2	$\left(\frac{2}{9}\right)^{1/6} \frac{1}{4\sqrt{\epsilon}} \approx 8.7013 \times 10^{-1}$	$\frac{\tan^2\theta}{2} \approx 3.7856 \times 10^{-1}$	$-\tan\theta$	0	0

Table 3 Values of several numerical parameters for each simulation set, where T is the total simulation time defined as $T = t_{\text{end}} - t_0$ with $t_0 = 0$ s

Simulation	L_x (m)	L_y (m)	L_z (m)	T (s)	N_x	N_y	N_z	Running time (min)
PFE-SP2: CG2/Δt	4110.90	16,000	20	1713.4	124	480	4	956 (1044/1058)
PFE-SP2: CG2/$\frac{\Delta t}{2}$	4110.90	16,000	20	1713.4	124	480	4	1350.1
PFE-SP2: CG2/$\frac{\Delta t}{4}$	4110.90	16,000	20	1713.4	124	480	4	2621.9
PFE-SP2: CG4/Δt	4110.90	16,000	20	1713.4	62	240	2	1422.5

The time step is $\Delta t \approx 0.2855$ s. Degrees of freedom n_{DOF} scale as $n_{\text{CG}} N_x (n_{\text{CG}} N_y + 1)$ with N_x cells and N_y cells in the x, y-directions. Hence, when $n_{\text{CG}} N_x$ and $n_{\text{CG}} N_Y$ are fixed, n_{DOF} remains the same. Last column: run times of simulations computed on 40 cores of Leeds' arc4-HPC (Macbook with 12 cores using $\hat{\phi} = 1$; 1055 min with $\hat{\phi}(z)$ GLL2)

Finally, the above set-up made it possible to conduct four simulations using the two-soliton solution at $t = 0$ as initial condition, while varying the time step and basis functions. Two basis functions have been used: second-order and fourth-order Gauss–Lobatto–Legendre (GLL) polynomials, respectively, denoted by CG2 and CG4. The simulations using CG2 have been repeated for three sequentially halved time steps $(1, 1/2, 1/4)\Delta t$ at the same spatial resolution, while the simulation with CG4 has lower resolution but the same degrees-of-freedom as the CG2 one, with time step $\Delta t =\approx 0.2855s$. The two-soliton parameter values used are provided in Table 2. Simulation data are given in Table 3, including run times. The initial conditions and final fields shown in Fig. 15 reveal the periodicity of the perturbation velocity potential $\tilde{\psi}$ as well as the amplification achieved.

Further simulation results are summarised in Fig. 16. All simulations appear to be stable, as can be discerned from the two energy plots (Fig. 16b, d), which demonstrate a second-order accuracy in time. Both simulations with time step Δt are similar with CG4 showing slightly higher energy oscillations. The maximum amplification is established by the ratio of the maximum amplitude over the far-field amplitude versus time; it eventually straddles between 3.85 and 4.05. Recall that the exact KPE solution has a fixed fourfold amplification. The shown mild increase of the maximum amplification over time seems to be caused by the slow decay, due to dispersion effects, of the far-field soliton amplitude, here taken as the maximum at $y = 13{,}000$ m. That mild increase does not correlate with the energy oscillations, since the four simulations show similar amplification patterns, while the energy oscillations clearly diminish strongly for smaller time steps. Hence, the set of simulations together demonstrate the robustness of the results. It took some computational effort to attain the spatial–temporal resolution required to successfully simulate the approximately fourfold amplification in this two-soliton travelling solution with the PFE. In context, recall that previous numerical

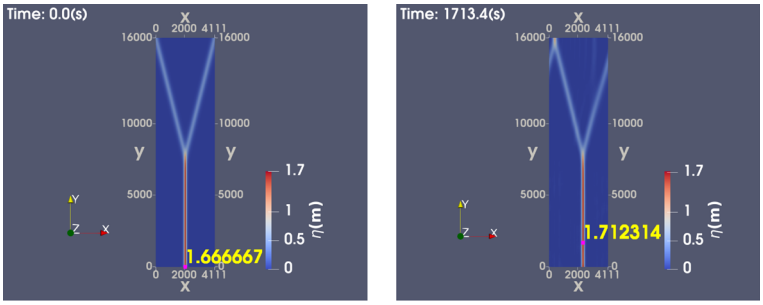

(a) Initial condition for η_0 (b) η at $t_{end} = 1713.4$

(c) Initial condition for $\tilde{\psi}_0$ (d) $\tilde{\psi}$ at $t_{end} = 1713.4$

Fig. 15 Initial conditions for **a** η_0 and **c** $\tilde{\psi}$ in the potential-flow simulation with two interacting solitons (PFE-SP2) simulation with $\epsilon = 0.05$, employing finite-element polynomials of order CG2 and a time step $\frac{\Delta t}{2} \approx 0.1427$ s. Panel **b** and **d** show the numerical solutions at $t_{\text{end}} = 1713.4$ s. All axes and η have units of m, time has unit s, and ϕ has unit of m^2/s. Other parameters take the values $\tilde{A} = k_4^2/2 = 0.38$ with $k_4 = (2/9)^{1/6}/(4\sqrt{\epsilon})$. Note that this yields a 0.38 m soliton with width ~ 200 m for a depth of $H_0 = 20$ m. The fourfold soliton then has an amplitude of circa 1.6 m across 400 m

simulations revealed amplifications of [3.6, 3.9] in different set-ups employing the more dispersive BLE [11, 13, 23].

B.3 SP3: Three Interacting Solitons

Initial conditions (12) and (13) for the BLE are transformations of a KPE solution of three-soliton interactions (SP3) with possible proven maximum of ninefold amplification of the far-field incoming solitons. Again, using (9), the function $K(X, Y, \tau)$ found from (23) reads

$$
\begin{aligned}
K(X, Y, \tau) &= 2\mathrm{e}^{(k_4^2+k_5^2+k_6^2)Y} \\
&\times \Big(A_{135}\, \mathrm{e}^{-\alpha} \cosh\Big(-3k_4 X + (k_4^3 + k_6^3 - k_5^3)\tau + \alpha\Big) \\
&+ 2A_{136}\, \mathrm{e}^{(k_6^2-k_5^2)Y^*} \cosh\left(k_4 X - k_4^3 \tau\right) \cosh\Big((k_6^2 - k_5^2)(Y - Y^*)\Big) \\
&+ A_{236} \mathrm{e}^{\alpha} \cosh\Big(k_4 X + (k_4^3 + k_5^3 - k_6^3)\tau - \alpha\Big)\Big),
\end{aligned}
\tag{B24}
$$

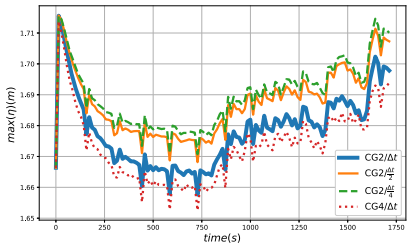

(a) Maximum values of η

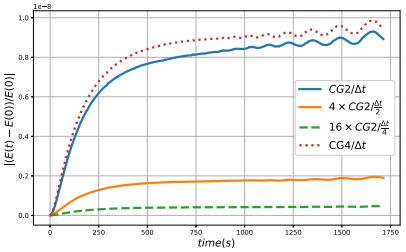

(b) Relative energy error

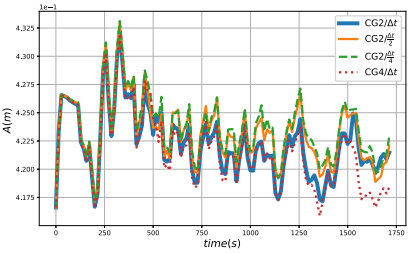

(c) A over time

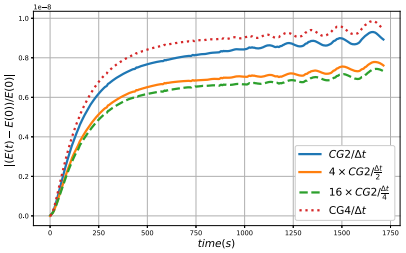

(d) Relative energy error, re-scaled for CG2-$\Delta t/2$ and CG2-$\Delta t/4$

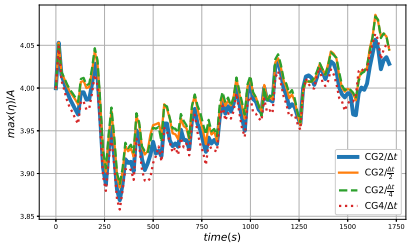

(e)max/A over time

Fig. 16 Results from four potential-flow simulations with two-soliton interactions (PFE-SP2) using order CG2 basis functions with time step $\Delta t(1, 1/2, 1/4)$—respectively, indicated by blue, orange, and green dashed lines—and order CG4 basis functions with time step Δt (red dotted lines), Shown are: **a** maximum values of η over time. **b** Relative-energy error $|1 - E(t)/E(0)|$ in time. All the initial total energies $E(0)$ are the same, -2.5803×10^{12} up to six digits. **c** $A := \max_x(\eta(\cdot, y = 13{,}000, t))$. **d** Relative energy error for CG2 (computed with six digits) with the $\Delta t/2$ result multiplied by 4 and the $\Delta t/4$ result multiplied by 16 to highlight the temporal near-convergence. **e** The amplification displayed is the maximum value of η divided by A over time

with $e^{-\alpha} = \sqrt{(ac)}$, such that $\alpha = -\ln\sqrt{ac}$ and

$$k_5 - k_4 - k_6 = -3k_4, \quad k_6 - k_5 - k_4 = k_4. \tag{B25}$$

Herein, we use Eq. (17). Furthermore, we derive

$$K_X = 2k_4 e^{(k_4^2+k_5^2+k_6^2)Y}$$

$$\times \left(-3A_{135}\mathrm{e}^{-\alpha}\sinh\left(-3k_4X+(k_4^3+k_6^3-k_5^3)\tau+\alpha\right)\right.$$
$$+2A_{136}\mathrm{e}^{(k_6^2-k_5^2)Y^*}\sinh\left(k_4X-k_4^3\tau\right)\cosh\left((k_6^2-k_5^2)(Y-Y^*)\right)$$
$$\left.+A_{236}\mathrm{e}^{\alpha}\sinh\left(k_4X+(k_4^3+k_5^3-k_6^3)\tau-\alpha\right)\right) \tag{B26a}$$

$$K_{XX}=2k_4^2\mathrm{e}^{(k_4^2+k_5^2+k_6^2)Y}$$
$$\times \left(9A_{135}\mathrm{e}^{-\alpha}\cosh\left(-3k_4X+(k_4^3+k_6^3-k_5^3)\tau+\alpha\right)\right.$$
$$+2A_{136}\mathrm{e}^{(k_6^2-k_5^2)Y^*}\cosh\left(k_4X-k_4^3\tau\right)\cosh\left((k_6^2-k_5^2)(Y-Y^*)\right)$$
$$\left.+A_{236}\mathrm{e}^{\alpha}\cosh\left(k_4X+(k_4^3+k_5^3-k_6^3)\tau-\alpha\right)\right) \tag{B26b}$$

$$K_{XXX}=2k_4^3\mathrm{e}^{(k_4^2+k_5^2+k_6^2)Y}$$
$$\times \left(-27A_{135}\mathrm{e}^{-\alpha}\sinh\left(-3k_4X+(k_4^3+k_6^3-k_5^3)\tau+\alpha\right)\right.$$
$$+2A_{136}\mathrm{e}^{(k_6^2-k_5^2)Y^*}\sinh\left(k_4X-k_4^3\tau\right)\cosh\left((k_6^2-k_5^2)(Y-Y^*)\right)$$
$$\left.+A_{236}\mathrm{e}^{\alpha}\sinh\left(k_4X+(k_4^3+k_5^3-k_6^3)\tau-\alpha\right)\right) \tag{B26c}$$

$$K_Y=(k_4^2+k_5^2+k_6^2)K$$
$$+4A_{136}(k_6^2-k_5^2)\mathrm{e}^{(k_4^2+k_5^2+k_6^2)Y}\mathrm{e}^{(k_6^2-k_5^2)Y^*}$$
$$\times\cosh\left(k_4X-k_4^3\tau\right)\sinh\left((k_6^2-k_5^2)(Y-Y^*)\right) \tag{B26d}$$

$$K_{YY}=(k_4^2+k_5^2+k_6^2)K_Y$$
$$+4A_{136}(k_4^2+k_5^2+k_6^2)(k_6^2-k_5^2)\mathrm{e}^{(k_4^2+k_5^2+k_6^2)Y}\mathrm{e}^{(k_6^2-k_5^2)Y^*}$$
$$\times\cosh\left(k_4X-k_4^3\tau\right)\sinh\left((k_6^2-k_5^2)(Y-Y^*)\right)$$
$$+4A_{136}(k_6^2-k_5^2)^2\mathrm{e}^{(k_4^2+k_5^2+k_6^2)Y}\mathrm{e}^{(k_6^2-k_5^2)Y^*}$$
$$\times\cosh\left(k_4X-k_4^3\tau\right)\cosh\left((k_6^2-k_5^2)(Y-Y^*)\right) \tag{B26e}$$

$$K_{XY}=(k_4^2+k_5^2+k_6^2)K_X$$
$$+4k_4A_{136}(k_6^2-k_5^2)\mathrm{e}^{(k_4^2+k_5^2+k_6^2)Y}\mathrm{e}^{(k_6^2-k_5^2)Y^*}$$
$$\times\sinh\left(k_4X-k_4^3\tau\right)\sinh\left((k_6^2-k_5^2)(Y-Y^*)\right) \tag{B26f}$$

$$K_{XYY}=(k_4^2+k_5^2+k_6^2)K_{XY}$$
$$+4k_4A_{136}(k_4^2+k_5^2+k_6^2)(k_6^2-k_5^2)\mathrm{e}^{(k_4^2+k_5^2+k_6^2)Y}\mathrm{e}^{(k_6^2-k_5^2)Y^*}$$
$$\times\sinh\left(k_4X-k_4^3\tau\right)\sinh\left((k_6^2-k_5^2)(Y-Y^*)\right)$$
$$+4k_4A_{136}(k_6^2-k_5^2)^2\mathrm{e}^{(k_4^2+k_5^2+k_6^2)Y}\mathrm{e}^{(k_6^2-k_5^2)Y^*}$$
$$\times\sinh\left(k_4X-k_4^3\tau\right)\cosh\left((k_6^2-k_5^2)(Y-Y^*)\right). \tag{B26g}$$

As before in SP2, we use these relations (B26) in (B23).

The size of the periodic channel in KPE is determined by taking $Y_1 = Y_\star$ and $Y_2 = Y_1 + \Delta Y$, where we choose the BLE scaling $\Delta\hat{y} = 47 = \Delta Y \mu(\sqrt{2}/3)^{\frac{2}{3}}/\epsilon$ and a(n initial) time τ_0. The periodicity of the channel is then determined using the $[1, 2]^+$ and $[5, 6]^-$ limiting branches in (19) to find that

$$X_2 = (k_6 + k_5)Y_2 + (k_6^2 + k_5k_6 + k_5^2)\tau_0 - \frac{1}{(k_6 - k_5)} \ln\left(\frac{A_{246}}{A_{146}}\right) \tag{B27a}$$

$$X_1 = -(k_6 + k_5)Y_2 + (k_6^2 + k_5k_6 + k_5^2)\tau_0 - \frac{1}{(k_6 - k_5)} \ln\left(\frac{A_{136}}{A_{135}}\right). \tag{B27b}$$

Using the scalings then leads to expressions for $x_{1,2}$.

Appendix C: Variational Numerical Discretisation of BLE and PFE

C.1 Coordinate Transformation PFE

The adapted Luke VP's (41b) is transformed from $\{x, y, z, t\}$ coordinates to new coordinates

$$\hat{x} = x, \quad \hat{y} = y, \quad \hat{t} = t, \quad \hat{z} = \frac{zH_0}{h(x, y, t)}, \tag{C28}$$

with $\hat{x} \in [x_1, x_2]$, $\hat{y} \in [y_1, y_2]$ and $\hat{z} \in [0, H_0]$, such that the transformed domain is fixed. Hence, the non-zero entries in the Jacobian are

$$\hat{x}_x = 1, \quad \hat{y}_y = 1, \quad \hat{t}_t = 1, \tag{C29}$$

$$\hat{z}_x = -\frac{\hat{z}}{h}h_{\hat{x}}, \quad \hat{z}_y = -\frac{\hat{z}}{h}h_{\hat{y}}, \quad \hat{z}_z = \frac{H_0}{h(\hat{x}, \hat{y}, \hat{t})}, \quad \hat{z}_t = -\frac{\hat{z}}{h}h_{\hat{t}}. \tag{C30}$$

The transformation rules therefore become

$$\partial_x = \partial_{\hat{x}} - \frac{\hat{z}}{h}h_{\hat{x}}\partial_{\hat{z}}, \tag{C31a}$$

$$\partial_y = \partial_{\hat{y}} - \frac{\hat{z}}{h}h_{\hat{y}}\partial_{\hat{z}}, \tag{C31b}$$

$$\partial_z = \frac{H_0}{h}\partial_{\hat{z}}, \tag{C31c}$$

$$\partial_t = \partial_{\hat{t}} - \frac{\hat{z}}{h}h_{\hat{t}}\partial_{\hat{z}}, \tag{C31d}$$

$$|J| = |\hat{J}^{-1}| = \frac{h}{H_0}, \tag{C31e}$$

$$\mathrm{d}x\,\mathrm{d}y\,\mathrm{d}z\,\mathrm{d}t = \frac{h}{H_0}\,\mathrm{d}\hat{x}\,\mathrm{d}\hat{y}\,\mathrm{d}\hat{z}\,\mathrm{d}\hat{t}, \tag{C31f}$$

with Jacobian $\hat{J} = \partial(\hat{x}, \hat{y}, \hat{z}, \hat{t})/\partial(x, y, z, t)$, $J = \hat{J}^{-1}$ and determinant $|J|$. Consequently, after dropping all hats and tildes, the adapted Luke's VP (41b) transforms as follows:

$$
\begin{aligned}
0 = \delta \int_0^T \int_{x_1}^{x_2} \int_{y_1}^{y_2} \int_0^{H_0} & \frac{h}{H_0}(\partial_t \phi - \frac{z}{h}\partial_t h \partial_z \phi) \\
& + \frac{1}{2}\frac{h}{H_0}(U_0 + \partial_x \phi - \frac{z}{h}\partial_x h \partial_z \phi)^2 \\
& + \frac{1}{2}\frac{h}{H_0}\left(x\partial_y U_0 + \partial_y \phi - \frac{z}{h}\partial_y h (x\partial_z U_0 + \partial_z \phi)\right)^2 \\
& + \frac{1}{2}\frac{H_0}{h}(x\partial_z U_0 + \partial_z \phi)^2 \\
& + g\left(z\frac{h}{H_0} - H_0\right)\frac{h}{H_0}\,\mathrm{d}z\,\mathrm{d}x\,\mathrm{d}y\,\mathrm{d}t \qquad \text{(C32)} \\
= -\delta \int_0^T \int_{x_1}^{x_2} \int_{y_1}^{y_2} & \psi \partial_t h - \frac{1}{2}gh^2 + ghH_0\,\mathrm{d}x\,\mathrm{d}y \\
- \int_{x_1}^{x_2} \int_{y_1}^{y_2} \int_0^{H_0} & \frac{1}{2}\frac{h}{H_0}(U_0 + \partial_x \phi - \frac{z}{h}\partial_x h \partial_z \phi)^2 \\
& + \frac{1}{2}\frac{h}{H_0}\left(x\partial_y U_0 + \partial_y \phi - \frac{z}{h}\partial_y h (x\partial_z U_0 + \partial_z \phi)\right)^2 \\
& + \frac{1}{2}\frac{H_0}{h}(x\partial_z U_0 + \partial_z \phi)^2\,\mathrm{d}z\,\mathrm{d}x\,\mathrm{d}y\,\mathrm{d}t, \qquad \text{(C33)}
\end{aligned}
$$

with free-surface potential $\psi(x, y, t) = \phi(x, y, H_0, t)$, this final expression for the VP being obtained using integration by parts of the first and second terms with respect to time and z, as well as the cancellation $\delta \int_0^{H_0} h\phi/H_0|_0^T\,\mathrm{d}z = 0$ using end-point conditions of the variations in time. Also, note that $U_0 = U_0(y, zh/H_0)$ in which z is really $\hat{z}$, whose hat was hitherto dropped.

The next step is to partition the (perturbation) velocity potential further into a free-surface and interior part

$$
\phi(x, y, z, t) = \psi(x, y, t)\hat{\phi}(z) + \varphi(x, y, z, t), \qquad \text{(C34)}
$$

with $\hat{\phi}(H_0) = 1$ and a homogeneous Dirichlet condition $\varphi(x, y, H_0, t) = 0$, such that $\phi(x, y, H_0, t) = \psi(x, y, z, t)$. Consequently, VP (C33) becomes

$$
\begin{aligned}
0 = -\delta \int_0^T \int_{x_1}^{x_2} \int_{y_1}^{y_2} & \psi \partial_t h - \frac{1}{2}gh^2 + ghH_0\,\mathrm{d}x\,\mathrm{d}y \\
- \int_{x_1}^{x_2} \int_{y_1}^{y_2} \int_0^{H_0} & \frac{1}{2}\frac{h}{H_0}(U_0 + \hat{\phi}\partial_x \psi + \partial_x \varphi - \frac{z}{h}\partial_x h(\psi \partial_z \hat{\phi} + \partial_z \varphi))^2 \\
& + \frac{1}{2}\frac{h}{H_0}\left(x\partial_y U_0 + \hat{\phi}\partial_y \psi + \partial_y \varphi\right.
\end{aligned}
$$

$$-\frac{z}{h}\partial_y h(x\partial_z U_0 + \psi\partial_z\hat{\phi} + \partial_z\varphi)\Big)^2 + \frac{1}{2}\frac{H_0}{h}\Big(x\partial_z U_0 + \psi\partial_z\hat{\phi} + \partial_z\varphi\Big)^2 \,\mathrm{d}z\,\mathrm{d}x\,\mathrm{d}y\,\mathrm{d}t, \tag{C35}$$

with $U_0 = U_0(y, zh/H_0)$.

C.2 Time-Discrete VPs for BLE

Hereafter dropping tildes on all variables, a second-order fully implicit modified-midpoint (MMP, [31]) time-discrete version of VP (42b) is

$$\begin{aligned} 0 = \delta \iint_{\Omega_h} & \eta^{n+1/2}\frac{(\Phi^{n+1}-\Phi^n)}{\Delta t} - \Phi^{n+1/2}\frac{(\eta^{n+1}-\eta^n)}{\Delta t} \\ & + \frac{\mu}{2}\nabla\eta^{n+1/2}\cdot\frac{(\nabla\Phi^{n+1}-\nabla\Phi^n)}{\Delta t} - \frac{\mu}{2}\nabla\Phi^{n+1/2}\cdot\frac{(\nabla\eta^{n+1}-\nabla\eta^n)}{\Delta t} \\ & + \frac{1}{2}(1+\epsilon\eta^{n+1/2})|\nabla(U_0x+\Phi^{n+1/2})|^2 + \frac{1}{2}(\eta^{n+1/2})^2 \\ & + \mu\Big(\nabla q^{n+1/2}\cdot\nabla(U_0x+\Phi^{n+1/2}) - \frac{3}{4}(q^{n+1/2})^2\Big)\,\mathrm{d}x\,\mathrm{d}y. \end{aligned} \tag{C36}$$

The weak formulations arise by taking partial variational derivatives of (C36) with respect to $\{\eta^{n+1/2}, \Phi^{n+1/2}, q^{n+1/2}\}$. This yields a fully coupled system of three equations after we eliminate the variables η^{n+1} and Φ^{n+1} in these equations, so not in the VP, via

$$\eta^{n+1} = 2\eta^{n+1/2} - \eta^n, \quad \Phi^{n+1} = 2\Phi^{n+1/2} - \Phi^n. \tag{C37}$$

Subsequently, once $\{\eta^{n+1/2}, \Phi^{n+1/2}, q^{n+1/2}\}$ are determined, these relations are also used to recover the updates. The above procedure is a shortcut from a more extensive time-discrete VP that fully recovers the MMP scheme [32].

A second-order partially implicit Störmer–Verlet time-discrete version SV1-BLE of the VP (42b) (e.g., the time-discrete VP for (52) in [12] is written down and used) is

$$\begin{aligned} 0 = \delta \iint_{\Omega_h} & \eta^{n+1/2}\frac{(\Phi^{n+1}-\Phi^n)}{\Delta t} - \eta^{n+1}\frac{\Phi^{n+1}}{\Delta t} + \eta^n\frac{\Phi^n}{\Delta t} \\ & + \frac{\mu}{2}\nabla\eta^{n+1/2}\cdot\frac{(\nabla\Phi^{n+1}-\nabla\Phi^n)}{\Delta t} \\ & - \frac{\mu}{2}\nabla\eta^{n+1}\cdot\frac{\nabla\Phi^{n+1}}{\Delta t} + \frac{\mu}{2}\nabla\eta^n\cdot\frac{\nabla\Phi^n}{\Delta t} \\ & + \frac{1}{4}(1+\epsilon\eta^{n+1/2})(|\nabla(U_0x+\Phi^n)|^2 + |\nabla(U_0x+\Phi^{n+1})|^2) \\ & + \frac{1}{2}(\eta^{n+1/2})^2 + \frac{1}{2}\mu\Big(\nabla q^n\cdot\nabla(U_0x+\Phi^n) - \frac{3}{4}(q^n)^2\Big) \end{aligned}$$

$$+\frac{1}{2}\mu\Big(\nabla q^{n+1}\cdot\nabla(U_0x+\Phi^{n+1})-\frac{3}{4}(q^{n+1})^2\Big)\,\mathrm{d}x\,\mathrm{d}y, \tag{C38}$$

wherein variations are taken with respect to $\{\Phi^n;\, q^n;\, \eta^{n+1/2};\, \Phi^{n+1}\}$ in turn.

An adjoint alternative and partially implicit Störmer–Verlet time-discrete version SV2-BLE of VP (42b) (e.g., basically the time-discrete VP for (49) in [12] is written down and used) reads

$$\begin{aligned}
0=\delta\iint_{\Omega_h}&\eta^n\frac{(\Phi^{n+1/2}-\Phi^n)}{\Delta t}+\eta^{n+1}\frac{(\Phi^{n+1}-\Phi^{n+1/2})}{\Delta t}\\
&+\frac{\mu}{2}\nabla\eta^n\cdot\frac{(\nabla\Phi^{n+1/2}-\nabla\Phi^n)}{\Delta t}+\frac{\mu}{2}\nabla\eta^{n+1}\cdot\frac{(\nabla\Phi^{n+1}-\nabla\Phi^{n+1/2})}{\Delta t}\\
&+\frac{1}{4}(1+\epsilon\eta^n)|\nabla(U_0x+\Phi^{n+1/2})|^2\\
&+\frac{1}{4}(1+\epsilon\eta^{n+1})|\nabla(U_0x+\Phi^{n+1/2})|^2+\frac{1}{4}(\eta^n)^2+\frac{1}{4}(\eta^{n+1})^2\\
&+\mu\Big(\nabla q^{n+1/2}\cdot\nabla(U_0x+\Phi^{n+1/2})-\frac{3}{4}(q^{n+1/2})^2\Big)\,\mathrm{d}x\,\mathrm{d}y,
\end{aligned} \tag{C39}$$

wherein variations are taken with respect to $\{\eta^n;\, \Phi^{n+1/2};\, q^{n+1/2};\, \eta^{n+1}\}$ in turn. Note that both SV1-BLE and SV2-BLE are comprised of four evaluations, with the first three ones being implicit evaluations.

C.3 Time-Discrete MMP-VP for PFE

After applying the strategy for deriving the variational MMP [31], the time-discrete MMP-counterpart of VP (C35) emerges as follows:

$$\begin{aligned}
0=\delta\int_{x_1}^{x_2}\int_{y_1}^{y_2}&\psi^{n+1/2}\frac{(h^{n+1}-h^n)}{\Delta t}-h^{n+1/2}\frac{(\psi^{n+1}-\psi^n)}{\Delta t}\\
&-\frac{1}{2}g(h^{n+1/2})^2+gh^{n+1/2}H_0\,\mathrm{d}x\,\mathrm{d}y\\
&-\int_{x_1}^{x_2}\int_{y_1}^{y_2}\int_0^{H_0}\frac{1}{2}\frac{h^{n+1/2}}{H_0}\Big(U_0+\hat{\phi}\partial_x\psi^{n+1/2}+\partial_x\varphi^{n+1/2}\\
&-\frac{z}{h^{n+1/2}}\partial_xh^{n+1/2}(\psi^{n+1/2}\partial_z\hat{\phi}+\partial_z\varphi^{n+1/2})\Big)^2\\
&+\frac{1}{2}\frac{h^{n+1/2}}{H_0}\Big(x\partial_yU_0+\hat{\phi}\partial_y\psi^{n+1/2}+\partial_y\varphi^{n+1/2}\\
&-\frac{z}{h^{n+1/2}}\partial_yh^{n+1/2}(x\partial_zU_0+\psi^{n+1/2}\partial_z\hat{\phi}+\partial_z\varphi^{n+1/2})\Big)^2\\
&+\frac{1}{2}\frac{H_0}{h^{n+1/2}}\Big(x\partial_zU_0+\psi^{n+1/2}\partial_z\hat{\phi}+\partial_z\varphi^{n+1/2}\Big)^2\,\mathrm{d}z\,\mathrm{d}x\,\mathrm{d}y
\end{aligned} \tag{C40a}$$

together with

$$\psi^{n+1} = 2\psi^{n+1/2} - \psi^n, \quad h^{n+1} = 2h^{n+1/2} - h^n. \tag{C40b}$$

In the current numerical implementation, we have used the approximation that

$$U_0 = U_0(y, zh/H_0) \approx U_0(y, z), \tag{C41}$$

in which z is the transformed coordinate.

C.3.1 MMP-PFE Optimising Solver Parameters in Firedrake

To aid in finding pre-conditioners, we state the potential-flow equations (PFE) in transformed coordinates, cf. expressions (B9a), (B9b) and (B11) in [21] simplified by taking $L_w = L_x$, $W = L_x$, $U = 0$, $\tilde{R} = 0$, $V = L_x^2$ (see the notation in Gidel's thesis [21]) to match our settings

$$z = H_0: \quad h_t + h_x\phi_x + h_y\phi_y - \phi_z\frac{H_0}{h}(1 + (h_x)^2 + (h_y)^2) = 0 \tag{C42a}$$

$$z = H_0: \quad \phi_t + \frac{1}{2}(\phi_x^2 + \phi_y^2) - \frac{1}{2}\frac{H_0^2}{h^2}\phi_z^2\big(1 + (h_x)^2 + (h_y)^2\big) + g(h - H_0) = 0 \tag{C42b}$$

$$\begin{aligned}\Omega: \quad & \phi_{xx} + \phi_{yy} + \frac{H_0^2}{h^2}\phi_{zz} - \frac{z}{h}\big((h_{xx} + h_{yy})\phi_z + 2h_x\phi_{xz} + 2h_y\phi_{yz}\big) \\ & + 2\frac{z}{h^2}\phi_z\big((h_x)^2 + (h_y)^2\big) + \frac{z^2}{h^2}\big((h_x)^2 + (h_y)^2\big)\phi_{zz} = 0\end{aligned} \tag{C42c}$$

with the transformed and fixed domain $\Omega = [0, L_x] \times [0, L_y] \times [0, H_0]$. Upon using the partitioning $\phi(x, y, z, t) = \psi(x, y, t)\hat{\phi}(z) + \varphi(x, y, z, t)$ with $\hat{\phi}(H_0) = 1$, $\varphi(x, y, H_0, t) = 0$ and $h - H_0 = \eta$, the above PFE system becomes

$$z = H_0: \quad \eta_t + \eta_x\hat{\phi}\psi_x + \eta_y\phi_y - (\psi\hat{\phi}_z + \varphi_z)\frac{H_0}{(H_0 + \eta)}(1 + (\eta_x)^2 + (\eta_y)^2) = 0 \tag{C43a}$$

$$\begin{aligned}z = H_0: \quad & \psi_t + \frac{1}{2}(\psi_x^2 + \psi_y^2) \\ & - \frac{1}{2}\frac{H_0^2}{(H_0 + \eta)^2}(\psi\hat{\phi}_z + \varphi_z)^2\big(1 + (\eta_x)^2 + (\eta_y)^2\big) + g\eta = 0\end{aligned} \tag{C43b}$$

$$\begin{aligned}\Omega: \quad & \hat{\phi}\psi_{xx} + \hat{\phi}\psi_{yy} + \frac{H_0^2}{(H_0 + \eta)^2}(\psi\hat{\phi}_{zz} + \varphi_{zz}) \\ & - \frac{z}{(H_0 + \eta)}\big((\eta_{xx} + \eta_{yy})(\psi\hat{\phi}_z + \varphi_z) + 2\eta_x(\psi_z\hat{\phi}_z + \varphi_{xz}) \\ & + 2\eta_y(\psi_y\hat{\phi}_z + \varphi_{yz})\big)\end{aligned}$$

$$+2\frac{z}{(H_0+\eta)^2}(\psi\hat{\phi}_z+\varphi_z)\big((\eta_x)^2+(\eta_y)^2\big)$$
$$+\frac{z^2}{(H_0+\eta)^2}\big((\eta_x)^2+(\eta_y)^2\big)(\psi\hat{\phi}_{zz}+\varphi_{zz})=0, \tag{C43c}$$

noting that η, ψ are solved at $z = H_0$, while the Poisson equation for φ is solved in the interior Ω with a homogeneous Dirichlet boundary condition $\varphi(x, y, H_0, t) = 0$ at $z = H_0$; Neumann conditions at $z = 0$, $y = 0, L_y$; and the domain is periodic in x.

An additive Schwartz method (ASM) pre-conditioner [33] was used to speed up the code, leading to the following solver-parameter settings:

```
lines_parameters = {'ksp_type': 'gmres',
                    'ksp_monitor': None,
                    'ksp_converged_reason': None,
                    'pc_type': 'python',
                    'pc_python_type': 'firedrake.ASMStarPC',
                    'snes_lag_preconditioner_persists': None,
                    'snes_lag_preconditioner': 5,
                    'star_construct_dim': 2,
                    'star_sub_sub_pc_type': 'lu',
                    "star_sub_sub_pc_factor_mat_ordering_type":
                    "rcm"}
```

employed in solving the MMP-weak forms as follows:

```
    #  Step-1: solve h^(n+1/2) wrt psi^(n+1/2)
    psif_exprnl1 = fd.derivative(VP3dpf, psimp, du=vvmp0)
    psif_exprnl1 = fd.replace(psif_exprnl1, {psii: 2.0*psimp-psi_f})
    psif_exprnl1 = fd.replace(psif_exprnl1, {h_new: 2.0*hmp-h_old})

    #  Step-2: solve psi^(n+1/2) wrt hmp=h^(n+1/2)
    h_exprnl1 = fd.derivative(VP3dpf, hmp, du=vvmp1)
    h_exprnl1 = fd.replace(h_exprnl1, {psii: 2.0*psimp-psi_f})
    h_exprnl1 = fd.replace(h_exprnl1, {h_new: 2.0*hmp-h_old})

    #  Step-3: wrt varmp=varphi^(n+1/2) solve varmp=varphi^(n+1/2)
    phi_exprnl1 = fd.derivative(VP3dpf, varphimp, du=vvmp2)
    phi_exprnl1 = fd.replace(phi_exprnl1, {psii: 2.0*psimp-psi_f})
    phi_exprnl1 = fd.replace(phi_exprnl1, {h_new: 2.0*hmp-h_old})

    Fexprnl = psif_exprnl1+h_exprnl1+phi_exprnl1
    phi_combonl = fd.NonlinearVariationalSolver(fd.NonlinearVariationalProblem(Fexprnl,
    result_mixedmp, bcs = BC_varphi_mixedmp), solver_parameters=lines_parameters)
```

in which VP3dpf therein is the time-discrete VP (C40) with its unknowns psimp, hmp, varphimp as $\psi^{n+1/2}$, $\eta^{n+1/2}\varphi^{n+1/2}$. Herein, the rcm-option is intended to limit memory use, but it has a set-up overhead. In addition, the pre-conditioner is lagged to reuse its factorisation over multiple time steps. Overall, these settings resulted in an approximate speed-up of 8.75 with four cores on a MacBookPro and 3.7 with ten cores on the ARC4-HPC at the University of Leeds relative to the following solver settings, which in turn were faster than the default ones:

```
    param_psicg = {'snes_atol': 1e-12,
    'ksp_converged_reason':None, "ksp_rtol": 1e-8,
    'fieldsplit_0_ksp_type': 'gmres', 'fieldsplit_0_pc_type': 'ilu',
        'fieldsplit_1_ksp_type': 'gmres',
        'fieldsplit_1_pc_type': 'ilu',
        'fieldsplit_2_ksp_type': 'cg',
        'fieldsplit_2_pc_type':
        'gamg','pc_factor_mat_solver_type':'mumps',
        'snes_monitor':None, 'ksp_monitor':None}
```

```
phi_combonl = fd.NonlinearVariationalSolver(fd.NonlinearVariationalProblem(Fexprnl,
result_mixedmp, bcs = BC_varphi_mixedmp),
solver_parameters=param_psicg)
```

The line_parameters solver parameters are designed[5] to be scalable, which means that

- the number of iterations stays the same as a function of the resolution;
- the code gets faster when more cores are used—up to a, usually large, limit.

References

1. Nikolkina, I., Didenlenkova, I.: Rogue waves in 2006–2010. Nat. Hazards Earth Syst. Sci. **11**, 2913–2924 (2011)
2. Dysthe, K., Krogstard, H.E., Muller, P.: Oceanic rogue waves. Annu. Rev. Fluid Mech. **40**, 287–310 (2008)
3. Benetazzo, A., Ardhuin, F., Bergamasco, F., Cavaleri, L., Guimarães, P.V., Schwendeman, M., Sclavo, M., Thomson, J., Torsello, A.: On the shape and likelihood of oceanic rogue waves. Sci. Rep. **7**, 8276 (2017)
4. Häfner, D., Gemmrich, J., Jochum, M.: Real-world rogue wave probabilities. Sci. Rep. **11**, 10084 (2021)
5. Mori, N., Janssen, P.A.E.M.: On kurtosis and occurrence probability of freak waves. J. Phys. Oceanogr. **36**, 1471–1483 (2006)
6. Kodama, Y.: KP solitons in shallow water. J. Phys. A: Math. Theor. **43**, 434004 (2010)
7. Kadomtsev, B.B., Petviashvili, V.I.: The stability of solitary waves in weakly dispersive media. Dokl. Akad. Nauk SSSR **192**, 532–541 (1970)
8. Wang, W., Pakozdi, C., Kamath, A., Bihs, H.: A fully nonlinear potential flow wave modelling procedure for simulations of offshore sea states with various wave breaking scenarios. Appl. Ocean Res. **117**, 102898 (2021)
9. Benney, D., Luke, J.: On the interactions of permanent waves of finite amplitude. J. Math. Phys. **43**, 309–313 (1964)
10. Pego, R.L., Quintero, J.R.: Two-dimensional solitary waves for a Benney–Luke equation. Physica D **132**, 476–496 (1999)
11. Ablowitz, M.J., Curtis, C.W.: Conservation laws and web-solutions for the Benney–Luke equation. Proc. R. Soc. A **469**, 20120690 (2013)
12. Bokhove, O., Kalogirou, A.: Variational water wave modelling: from continuum to experiment. In: Bridges, T., Groves, M., Nicholls, D. (eds.) LMS Lecture Note Series, vol. 426, pp. 226–260. Cambridge University Press, Cambridge (2016)
13. Choi, J., Bokhove, O., Kalogirou, A., Kelmanson, M.A.: Numerical experiments on extreme waves through oblique-soliton interactions. Water Waves **4**, 139–179 (2022)
14. Kodama, Y.: KP solitons in shallow water. J. Phys. A: Math. Theor. **43**, 434–484 (2010)
15. Rathgeber, F., Ham, D.A., Mitchell, L., Lange, M., Luporini, F., Mcrae, A.T.T., Bercea, G., Markall, G.R., Kelly, P.H.J.: Firedrake: automating the finite element method by composing abstractions. ACM Trans. Math. Softw. (2016). https://doi.org/10.1145/2998441
16. Luke, J.C.: A variational principle for a fluid with a free surface. J. Fluid Mech. **27**, 395–397 (1967)
17. Balay, S., Abhyankar, S., Adams, M.F., Brown, J., Brune, P., Buschelman, K., Dalcin, L., Eijkhout, V., Gropp, W.D., Kaushik, D., Knepley, M.G., McInnes, L.C., Rupp, K., Smith, B.F., Zampini, S., Zhang, H., Zhang, H.: PETSc users manual. Technical Report ANL-95/11-Revision 3.7, Argonne National Laboratory (2016). http://www.mcs.anl.gov/petsc
18. Balay, S., Gropp, W.D., McInnes, L.C., Smith, B.F.: Efficient management of parallelism in object oriented numerical software libraries. In: Arge, E., Bruaset, A.M., Langtangen, H.P. (eds.) Modern Software Tools in Scientific Computing, pp. 163–202. Birkhäuser Press, Basel (1997)

[5] These solver-parameter settings have been designed by, leading to the pre-conditioner information provided via, Colin Cotter upon OB's request, after OB provided the system description.

19. Gagarina, E., Ambati, A.R., van der Vegt, J., Bokhove, O.: Variational space-time (dis)continuous Galerkin method for nonlinear free surface water waves. J. Comput. Phys. **275**, 459–483 (2014)
20. Gagarina, E., Ambati, V.R., Nurijanyan, S., van der Vegt, J.J.W., Bokhove, O.: On variational and symplectic time integrators for Hamiltonian systems. J. Comput. Phys. **306**, 370–389 (2016)
21. Gidel, F.: Variational water-wave models and pyramidal freak waves. PhD thesis, University of Leeds (2018). http://etheses.whiterose.ac.uk/21730/
22. Gidel, F., Lu, Y., Bokhove, O., Kelmanson, M.: Variational and numerical modelling strategies for cost-effective simulations of driven free-surface waves (2022). Preprint at https://eartharxiv.org/repository/view/3411/
23. Gidel, F., Bokhove, O., Kalogirou, A.: Variational modelling of extreme waves through oblique interaction of solitary waves: application to Mach reflection. Nonlinear Proc. Geophys. **24**, 43–60 (2017)
24. Black, J., Morimoto, Y.: A note on quadratic forms positive definite under linear constraints. Economica **35**, 205–206 (1968)
25. Chiang, A.C., Wainwright, K.: Fundamental Methods of Mathematical Economics. McGraw-Hill, New York (2005)
26. Alnaes, M.S.: UFL: a finite element form language. In: Logg, A., Mardal, K.-A., Wells, G.N. (eds.) Automated Solution of Differential Equations by the Finite Element Method. Springer, Berlin (2011)
27. Alnaes, M.S., Logg, A., Oelgaard, K.B., Rognes, M.E., Wells, G.N.: Unified Form Language: a domain-specific language for weak formulations of partial differential equations. Technical report (2013). https://arxiv.org/pdf/1211.4047.pdf
28. Lu, Y., Gidel, F., Choi, J., Bokhove, O., Kelmanson, M.: Variational numerical modelling strategies for simulating driven free-surface waves. Revision in preparation (2024)
29. Deconinck, B.: Canonical variables for multiphase solutions of the KP equation. Stud. Appl. Math. **104**, 229–291 (2000)
30. Kodama, Y.: Solitons in Two-dimensional Shallow Water. SIAM, Philadelphia (2018). (**Exercise 6.7**)
31. Bokhove, O.: Variational modified-midpoint time-stepping scheme. Technical report (2023)
32. Gagarina, E.: Variational approaches to water wave simulations. PhD thesis, University of Twente (2014)
33. Marchena-Menendez, J., Kirby, R.C.: Additive Schwartz methods for serendipity elements. SIAM J. Sci. Comput. **45**, 401–420 (2023)